Sensors, Features, and Machine Learning for Oil Spill Detection and Monitoring: A Review

Rami Al-Ruzouq [1,2,*], **Mohamed Barakat A. Gibril [2,3]**, **Abdallah Shanableh [1,2]**, **Abubakir Kais [1]**, **Osman Hamed [4]**, **Saeed Al-Mansoori [5]** and **Mohamad Ali Khalil [2]**

[1] Civil and Environmental Engineering Department, University of Sharjah, Sharjah 27272, UAE; shanableh@sharjah.ac.ae (A.S.); u16104986@sharjah.ac.ae (A.K.)

[2] GIS & Remote Sensing Center, Research Institute of Sciences and Engineering, University of Sharjah, Sharjah 27272, UAE; mbgibril@sharjah.ac.ae (M.B.A.G.); mkhalil@sharjah.ac.ae (M.A.K.)

[3] Department of Civil Engineering, Faculty of Engineering, Universiti Putra Malaysia, Serdang 43400, Malaysia

[4] Faculty of Science and Engineering, University of Wolverhampton, Wolverhampton WV1 1LY, UK; o.hamed@wlv.ac.uk

[5] Applications Development and Analysis Section (ADAS), Mohammed Bin Rashid Space Centre (MBRSC), Dubai 211833, UAE; Saeed.AlMansoori@mbrsc.ae

* Correspondence: ralruzouq@sharjah.ac.ae; Tel.: +971-6-505-0953

check for
updates

Abstract: Remote sensing technologies and machine learning (ML) algorithms play an increasingly important role in accurate detection and monitoring of oil spill slicks, assisting scientists in forecasting their trajectories, developing clean-up plans, taking timely and urgent actions, and applying effective treatments to contain and alleviate adverse effects. Review and analysis of different sources of remotely sensed data and various components of ML classification systems for oil spill detection and monitoring are presented in this study. More than 100 publications in the field of oil spill remote sensing, published in the past 10 years, are reviewed in this paper. The first part of this review discusses the strengths and weaknesses of different sources of remotely sensed data used for oil spill detection. Necessary preprocessing and preparation of data for developing classification models are then highlighted. Feature extraction, feature selection, and widely used handcrafted features for oil spill detection are subsequently introduced and analyzed. The second part of this review explains the use and capabilities of different classical and developed state-of-the-art ML techniques for oil spill detection. Finally, an in-depth discussion on limitations, open challenges, considerations of oil spill classification systems using remote sensing, and state-of-the-art ML algorithms are highlighted along with conclusions and insights into future directions.

Keywords: marine pollution; oil spill remote sensing; oil spill detection; SAR; dark spot detection; feature extraction; machine learning; deep learning

1. Introduction

Oil spills are generally characterized as the release of liquid petroleum hydrocarbons into the environment due to human activities [1]. Spillage commonly occurs in water, on ice, or land during oil exploration, production, transportation, refining, storage, and distribution [2]. For instance, oil spillage may occur from offshore oil platforms, refineries, pipelines, chemical plants, treatment facilities, and transportation accidents and deliberate oil discharges from ships, as well as oil disposal from energy production and operational errors. Accidents generally account for the massive oil spill incidents worldwide. Shipping accidents, particularly mishaps caused by oil tankers, release a significant amount of oil and pose a substantially higher threat to water ecosystems more than other

pollution sources [3,4]. According to the International Tanker Owners Pollution Federation (TIOPF), approximately 5.86 million tons of oil are lost globally as a consequence of oil tanker accidents [5].

A worldwide dependence on oil-based products has long existed, and the continuous spillage of petroleum residues from tanker operations, accidents, and other maritime sources contaminates many coastlines and beaches worldwide [6]. Oil products entering the marine environment have a wide range of long-term environmental impacts depending on their chemical and physical composition and concentration as well as other environmental factors. However, these products can have notable short-term implications on ecosystems, habitats, and wildlife. For instance, coastal and marine wildlife exposed to oil is susceptible to intermediate health problems and involves long-term changes to their physiology and behavior [7].

Chemical and physical properties of oil, such as surface tension, specific gravity, and viscosity, along with various circumstances relating to the time and location of accidents, oil volume, and atmospheric factors, affect the behavior of oil in water. When different kinds of oil are spilled on either land or water, many physical, chemical, and biological degradation processes begin to act on them. When crude oil is released, it spreads to form a thin film, called oil slick, on the water surface. Then, many natural processes, known as oil weathering, work together to degrade the oil slick [8]. As oil travels through aquatic environments, a range of chemical and physical processes, including wind, wave and current compression, spreading and diffusion of surfaces, sedimentation and dissolution into the water column, emulsification, evaporation, and photochemical, as well as biological degradation, can influence and change the oil characteristics [9,10]. The distinction between marine and terrestrial spills lies in the speed at which the oil moves or disperses and the consequent size of the affected area. Oil spills in the water are carried by wind and current and often over long distances. The prediction of oil spill on land can be accurate because of its significantly slow movement, usual downward flow, and accumulation in depressions [11]. Spill response knowledge is evidential, and past spill responses are continuously being discovered to learn the behavior of oil spills, verify the effectiveness of countermeasures, and provide relevant data on handling future spills in similar scenarios [12].

Monitoring and detection of oil slicks is a crucial part of contingency planning for oil spills. Precise detection of oil spills and prediction of their trajectories are beneficial to fisheries, wildlife, liability dispute resolutions, and resource management for monitoring and conserving the marine ecosystem [6]. Traditional oil spill monitoring techniques, such as aerial or field investigation, are costly and fail to achieve timely and efficient identification of oil spill areas. Given the wide coverage, synoptic views, and the frequency of acquiring multisensory data, satellite-based remote sensing (RS) has been extensively used in detecting and monitoring oil spills in the past few decades using various types of remotely sensed data (Section 2). Numerous review papers that focus on oil spill RS are available in the literature [13–18]. These studies discussed the utilization and advantages of using various sources of remotely sensed data and techniques for oil spill extraction. However, existing review studies have yet to address the adoption of state-of-the-art machine learning (ML) techniques for identifying oil spills/slicks. The synergetic use of RS technologies and ML algorithms to detect and monitor oil spill slicks has been examined and adopted in a wide spectrum of studies [19–27]. ML techniques have demonstrated an effective means to extract oil spills from remotely sensed data in a (semi)automatic manner. Massive amounts of data can be handled and integrated to enable timely decision making and the analysis of potential oil spill incidents. Recent related literature (2010–2020) on the recognition, identification, and detection of oil spills using remotely sensed data and ML algorithms is reviewed in this study. A review of 110 investigations on different components of ML classification systems for oil spill detection, including 79 journal papers, 29 conference papers, and 2 book chapters, was conducted in this study. First, the advantages and shortcomings of commonly used remote sensors in oil spill detection are highlighted. Second, the preprocessing chain of remotely sensed data for oil spill detection and commonly extracted and selected features for oil spill detection are presented. Various classical and advanced ML approaches for oil spill detection are summarized and analyzed. Finally, the challenges, considerations, and future trends of oil spill

systems are emphasized. Figure 1 shows the overall structure of developing and adopting ML models for oil spill detection. The remainder of this paper is organized as follows. Different sources of remotely sensed data are described in Section 2. Different stages of data preprocessing are discussed in Section 3. Feature extraction and selection are highlighted in Section 4. Classical and advanced ML techniques for identifying oil spills are analyzed in Section 5. Finally, conclusions are drawn and some considerations for improving oil spill detection are provided in Section 6.
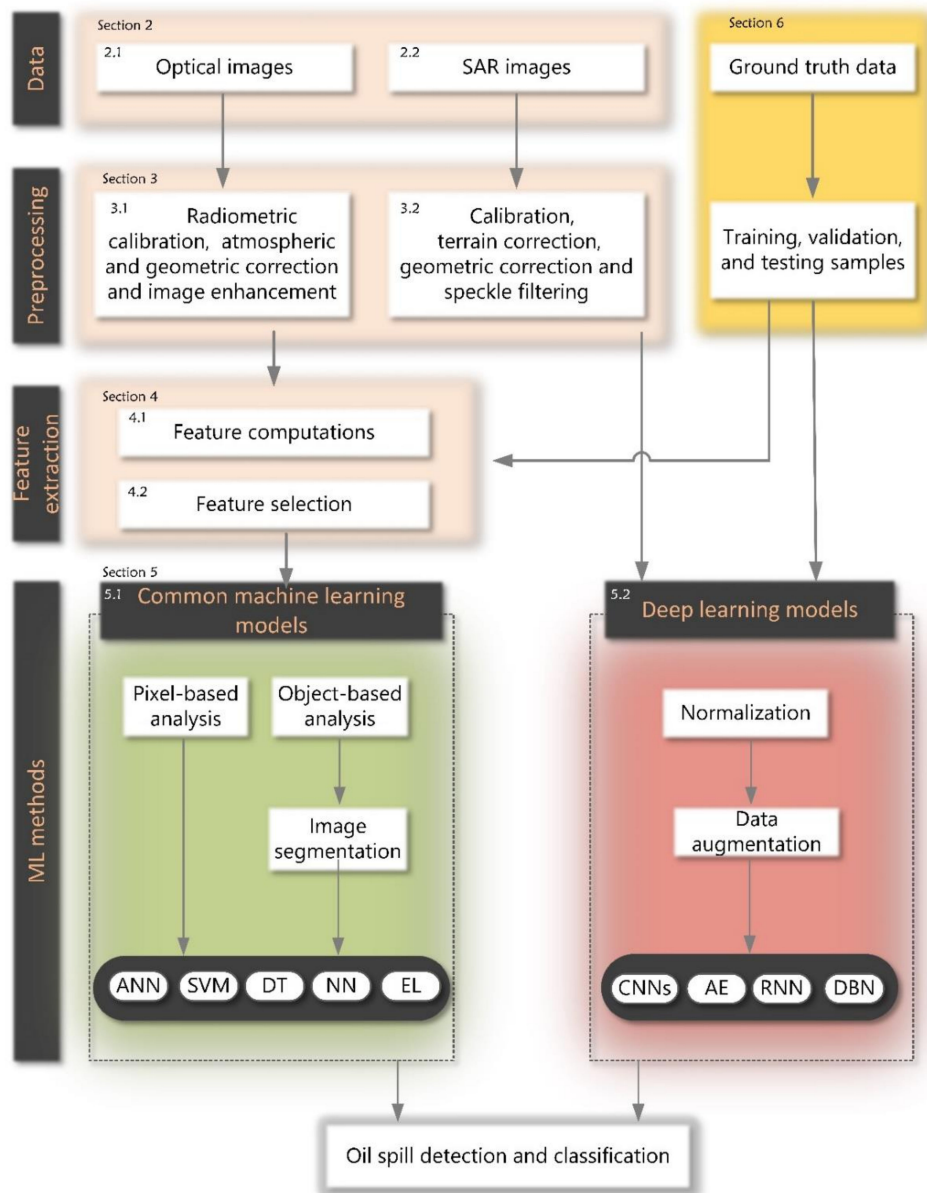

Figure 1. Framework of oil spill detection.

2. Remotely Sensed Data

Remotely sensed data are extensively used to detect and monitor oil spills in the past few decades. These data are generally acquired by passive and active systems. Passive sensors record naturally reflected and/or emitted solar radiation from the observed object, whereas active sensors use their energy source to illuminate sensed targets and record backscattered energy from the target. Visible and infrared multispectral, hyperspectral, thermal, microwave, and laser fluorosensors are some relevant remote sensing techniques for oil spill detection, monitoring, type characterization,

and thickness estimation. Given that each technique has its own advantages and shortcomings, acquiring essential information for timely and effective oil spill management from one source of data can be challenging [28,29]; thus, a concession exists when selecting potential technique(s) from others. The advantages and shortcomings of optical and microwave remote sensing data for oil spill detection and monitoring are discussed in the following sections.

2.1. Optical Data

Optical images are less widely used in oil spill studies compared to microwave images owing to their dependence on weather conditions and day light. Although the presence of cloud in skies and the lack of sunlight hinder the usage of optical sensors, these devices have a unique spectral characteristic that can fill the spatial and temporal gaps for a synoptic coverage of oil spills, provide valuable information to differentiate between oil spills and water surface features (i.e., algal blooms) [14,30,31], potentially identify oil spills at fine levels [32], and provide relative information for oil spill thickness estimation [28]. Passive remotely sensed data acquired at different regions of the electromagnetic spectrum, including the ultraviolet (100–400 nm), visible (VIS) (400–700 nm), and near-infrared (NIR) (750–1400 nm) regions, are used in detecting [30,32–40] and estimating oil spill surface thickness [31,41–45]. The utilization of multispectral data for oil spill detection is growing, and various satellite data with different resolutions are used in different studies, as shown in Table 1. Such studies used moderate-resolution imaging spectroradiometer [38,46–48], medium resolution imaging spectrometer (MODIS) [49], Sentinel-2 [36], Landsat [30,50,51], KOMPSAT-2 [52], and Gaofen-1 [51,53], among others. Figure 2 shows the different oil spill incidents captured by various optical satellites, such as Sentinel-2 (Figure 2a,b) and MODIS Terra and Aqua satellites (Figure 2c,d).
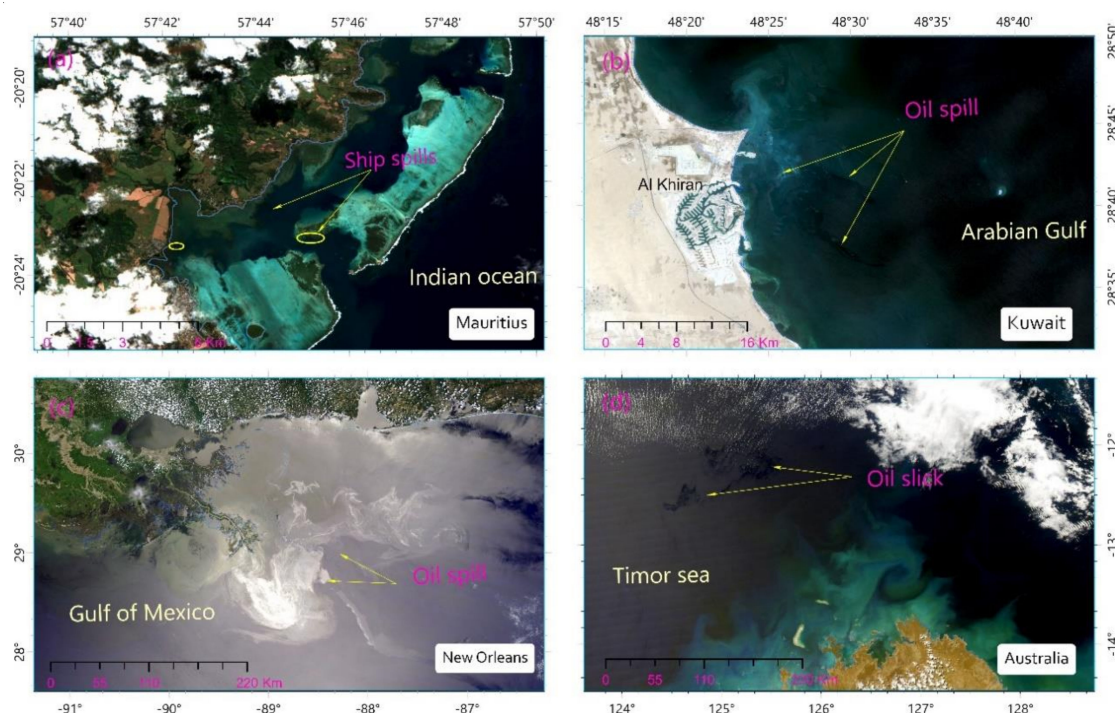

Figure 2. Oil spill incidents recognized from optical images: (**a**) Sentinel-2 image of ship spills near the coast of Mauritius on 10 August 2020, (**b**) Sentinel-2 image of massive oil slick off the coast of Kuwait on 11 August 2017, (**c**) NASA Terra satellite imagery of large oil spills on the Gulf of Mexico on 24 May 2010, and (**d**) NASA Aqua satellite image of oil slick in the Timor sea on 30 August 2009.

Spectral characteristics of oil spills may vary from one source to another depending on physical oil characteristics, film thickness, weather and illumination conditions, and optical properties of water column [36]. Although oil appears in the visible region of the spectra (approximately 400–700 nm) and exhibits relatively higher reflectance than water, it has no unique reflection/absorption features that can enable straightforward discrimination between oil and the background [15,54]. Nevertheless, in some special cases (i.e., Figure 2c), oil may look silvery with a greater reflectance than the background [54]. Moreover, heavy oil may look brown and peak between the 600 and 700 nm regions of the spectra, whereas mousse appears red-brown and peaks near 700 nm [55]. However, detectability of oil spills in images produced by visible sensors can be affected by the contrast between oil and water based on several factors, including illumination-view geometry (satellite and solar zenith angles), cloud coverage, sea state (wind speed), oil spectral properties (refractive index and absorption coefficient), and oil conditions and thickness [15,54,56].

The NIR bands (750–1400 nm) from sun-glittered satellite images for oil spill detection have been investigated in few studies. For instance, Pisano et al. [57] detected the marine oil spill from a MODIS near-infrared sun-glittered radiance imagery. Adamo et al. [58] reported that the NIR bands of MODIS and MEdium Resolution Imaging Spectrometer (MERIS) images show an increased performance of oil/non-oil class separability compared with the bands in the visible range. Moreover, the absorption features in the near-infrared NIR region have been used as a proxy for estimating the thickness of oil spill [41,42,49].

Table 1. List of optical satellites utilized in oil spill studies.

Satellite	Spectral Region (Bands)	Range (μm)	Spatial ResolUtion (m)	Revisit Time (Days)	Operation	References
MODIS (Terra, Aqua)	VIS, NIR, MIR, SWIR,55 LWIR (36 spectral bands)	B1–19 (0.405–2.155) B 20-36 (3.66–14.28)	250,500, 1000 m	1–2	1999/2002–operating	[38,46–48,59–62]
Landsat-8	VIS, NIR, SWIR, TIR (12 spectral bands)	B1–9 (0.43–1.38) B10–11 (10.6–12.51)	15, 30, 100 m	16	2013–operating	[51,63–67]
Landsat-7	VIS, NIR, MIR, TIR (8 spectral bands)	B1–5 (0.45–1.75) B6 (10.40–12.50) B7 (2.08–2.35)	15, 30, 60 m	16	1999–operating	[68–70]
Landsat-5	VIS, NIR, MIR, TIR (8 spectral bands)	B1–5 (0.45–1.75) B6 (10.40–12.50) B7 (2.08–2.35)	30, 120 m	16	1984–2013	[44,66,69]
Sentinel-2	VIS, NIR, SWIR (12 spectral bands)	0.443–2.190	10, 20, 60 m	5	2015–operating	[36,71,72]
KOMPSAT-2	VIS, NIR (5 bands)	0.45–0.9	1(pan), 4 m (MS)	14	2006–operating	[52]
Gaofen-1	VIS, NIR (5 bands)	0.45–0.89	2 (pan), 8 m (MS)	4	2013–operating	[51,53]
ASTER	VIS, NIR, SWIR, TIR (14 bands)	B1–3B (0.52–0.86) B4–B9 (1.6–2.43) B10–B14 (8.12–11.65)	15, 30, 90 m	4–16	1999–operating	[73–75]
Quickbird	VIS, NIR (5 bands)	0.45–0.9	0.61(pan), 2.4(MS)	1–3.5	2001–operating	[69,76]
Dubaisat-2	Visible, NIR (5 bands)	0.45–0.89	1(pan), 4 (MS)	<8	2013–operating	[63]
Huan Jing-1	VIS, NIR (4 bands)	0.43–0.90	30 m	4	2008–operating	[32,51,77]
RapidEye	VIS, NIR (4 bands)	0.44–0.85	5 m	1–5.5	2008–operating	[69]
WorldView-2	VIS, NIR (8 bands)	0.45–0.80	0.52(pan), 2.4(MS)	1.1	2009–operating	[44]
IKONOS	VIS, NIR (4 bands)	0.45–0.86	0.82(pan), 3.28(MS)	1–14	1999–2015	[69]
AVHRR (NOAA)	VIS, MIR, TIR(6 bands)	0.58–12.5	1.1 km	0.5	1978–operating	[74,78,79]
SeaWiFS	VIS, NIR (8 bands)	0.58–12.5	1.1–4.5 km	1	1997–2010	[80]
MERIS	VIS, NIR (15 bands)	0.4–0.95	300	3	2002–2012	[42,60]
SPOT-5	VIS, NIR, SWIR (4 bands)	B1–B3 (0.5–0.89) B4 (1.58–1.75)	2.5 or 5 m(Pan), 10(MS), 20(SWIR)	2–3	2002–2015	[44]

Visible (VIS), mid-wave infrared (MIR), shortwave infrared (SWIR), longwave infrared (LWIR), thermal (TIR), pan (panchromatic), MS (multispectral).

Hyperspectral remote sensing, also known as imaging spectroscopy, records reflected and/or emitted solar radiation in large number (hundreds) of contiguous narrow spectral bands ranging from 350 nm to 2500 nm. The absorption features of oil and other materials can be detected in hyperspectral images considering that a continuous and detailed spectrum is measured for each pixel. The high spectral resolution is vital considering the spectral similarity between diverse oil types, such as crude, diesel, lubricant, and kerosene, and subtle differences can be distinguished using hyperspectral RS technology [81]. Several studies on oil spills use hyperspectral systems, including airborne visible/infrared imaging spectrometry [22,23,82–87], Hyperion [81,88], and analytical spectral devices [89]. However, the requirement of advanced processing and analysis in hyperspectral images is a setback for real-time monitoring [15]. In addition, hyperspectral data are relatively expensive and publicly unavailable compared with multispectral and microwave images.

Oil, as a type of optically thick object, demonstrates different thermal characteristics (i.e., thermal conductivity, thermal inertia, and heat capacity) in comparison with surrounding water [90]. Given that oil absorbs and re-emits some parts of solar radiation as thermal energy, depending on the thickness of the oil slicks, it has a higher thermal infrared emissivity than water largely in the long-wavelength infrared spectral region (8000–14,000 nm) [54]. Temperature differences resulting from the variations in the emissivity enable the recognition of oil spills on sea surfaces. For instance, during sunny days, thick oil (greater than 500 μm thick) appears radiometrically hotter (brighter) in infrared images than the surrounding water due to its absorbance of greater amount of solar radiation; intermediate oil appears cooler (darker), while sheen (thin oil) and rainbow (very thin oil) are not detected [79,91]. Conversely, thick oil can appear cooler than the surrounding water at night because the heat loss of oil is faster than its surrounding water [91,92]. Considering that early morning and late afternoon are in-between periods, earlier in the afternoon could be a suitable time for oil film detection by thermal infrared sensors [93]. Various studies investigated the potential of using infrared bands for oil spill detection and monitoring from different remotely sensed data, including Landsat [94,95], Advanced Very High-Resolution Radiometer(AVHRR) [74,78,79,96], MODIS [97,98], Advanced Spaceborne Thermal Emission, and Reflection Radiometer (ASTER) [73,74], Environmental Satellite Advanced Along-Track Scanning Radiometer (ENVISAT-AATSR) [99], and thermal infrared imager [100]. One of the shortcomings of oil spill detection from thermal infrared images is that natural objects, such as shorelines, sediments, and organic matter, may appear like oil in thermal infrared images, which may cause errors to the detection of oil objects [15,16]. In addition, the resolution of satellite-based thermal images is low, and thermal images are often noisy and blurry [101].

2.2. SAR Data

Active microwave sensors are frequently used remote sensing systems for oil spill detection and monitoring due to their broad coverage and capabilities in collecting day-and-night data under all-weather conditions. Two main types of radar imaging are used in the detection and monitoring of oil spills, namely, synthetic aperture radar (SAR) and side-looking airborne radar (SLAR) systems. SAR (satellites-based), and SLAR (airborne) transmit/receive backscattered radio waves, and the reflection of target-surface properties are recorded to produce two-dimensional images of the scene. Both systems operate based on the same synthetic aperture principle and share the same side-looking imaging geometry. The usefulness and effectiveness of utilizing satellite-based SAR data for oil spill detection have been established in the reviewed literature. Table 2 lists the available satellite-based SAR system utilized in the reviewed literature on oil spills along with their frequencies and polarimetry.

The presence of oil in the sea typically reduces the intensity of the backscattered energy because oil dampens small-scale sea surface capillaries and short gravity waves [102,103]. Consequently, oil spills appear dark in SAR images. For example, Figure 3 depicts different oil spill incidents captured in various SAR images acquired in the Interferometric Wide (IW) swath mode and generated in high-resolution Level-1 ground range detected (GRD) format which entail radar observations projected

onto a regular 10 × 10 m grid. However, one challenge in using SAR images for oil spill detection is that oil spills are only one of other phenomena, such as manmade or natural events, which can reduce the scattering mechanism and appear dark in SAR images. These phenomena are known as lookalikes, which may include the following: natural surface films produced by plankton or fish, grease, floating algae, internal waves, low-wind areas, plant oil, ship wakes, and convergence zones.
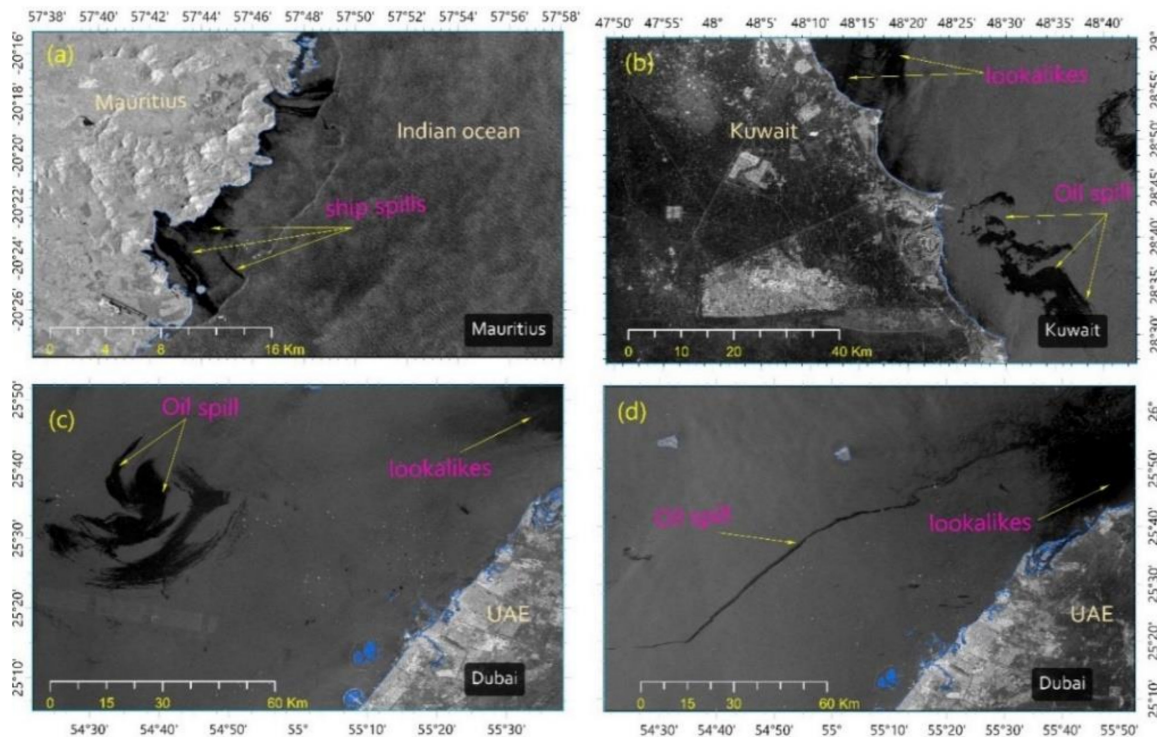

Figure 3. Oil spill incidents recognized from microwave Sentinel-1 images: (**a**) ship spills near the coast of Mauritius on 10 August 2020, (**b**) massive oil slick off the coast of Kuwait on 10 August 2017, (**c**) large oil spills detected on the Arabian Gulf on 8 March 2017, and (**d**) extended oil spill near the coast of United Arab Emirates on 10 October 2017.

The appearance of oil spills may vary in SAR images because the radiometric characteristics of radar imaging can differ based on the option of wavelengths, frequencies, and polarizations. L (wavelength of 24 cm), C (wavelength of 6 cm), and X (wavelength of 3 cm) are commonly used microwave bands in oil spill detection. This review found that the C-band is widely used in radar imagery for detecting oil spills, followed by X- and L-bands. SAR systems operate in different polarization schemes (VV, HH, VH, and HV). This condition enables the extraction of unique information for oil spill detection and monitoring. For instance, Sentinel-1 and Radarsat-2 can provide dual-polarized SAR data, that is, HH (horizontal transmitting and receiving) + HV (horizontal transmitting and vertical receiving) or VV+VH. Polarization modes can be single (i.e., HH or HV), dual (i.e., HH/HV or VV/VH), and quad (HH, HV, VH, and VV). However, some features can only be observed using specific polarizations. For example, an oil spill incident can be seen on the VV band of Sentinel-1 data, but it may not be visible in the corresponding VH band.

Table 2. List of SAR-equipped satellites utilized in the oil spill detection community.

Satellite Name	Operation	Operator	Band	Polarization	References
ERS-1, ERS-2	1991–2000, 1995–2011	European Space Agency (ESA)	C	Single-VV	[64,104–113]
RADARSAT-1	1995–2013	Canadian Space Agency (CSA)	C	Single-HH	[64,112,114–117]
RADARSAT-2	2007	Canadian Space Agency (CSA)	C	Quad	[26,64,106,110, 114,116,118–130]
ENVISAT ASAR	2002–2012	European Space Agency (ESA)	C	Dual	[64,77,105,106, 108–110,112,117, 124,129,131–144]
ALOS PALSAR, ALOS-2	2006–2011, 2013	Japan Aerospace Exploration Agency (JAXA)	L	Quad	[117,118,126,141, 143]
TerraSARX	2007	German Aerospace Centre	X	Quad	[112,145–150]
Cosmo Skymed-1/2	2007/2010	Italian Space Agency	X	Dual	[151–153]
RISAT-1	2012	India	C	Quad	[154–156]
Huan Jing-1C (HJ-1C)	2012	China	S	Single-VV	[157,158]
Kompsat-5	2013	Korea	X	Dual	[159,160]
Sentinel-1	2014	European Space Agency (ESA)	C	Dual	[64,65,161–165]

3. Data Preprocessing

3.1. Optical Images

Given the inherent radiometric and geometric errors of optical and SAR sensors and the strong effect of the environmental conditions, the preprocessing of remotely sensed data is a fundamental step in enhancing the data quality and improving the accuracy of the developed oil spill classification systems. The preprocessing chain of optical data may vary on the basis of the quality of the data source and the required level of processing for the analysis (i.e., levels 0, 1B, and 1C). This process can generally be categorized into five main steps, namely, radiometric calibration, atmospheric correction, geometric correction, image enhancement, and masking. The radiometric correction of optical images is required to mitigate the atmospheric effects to improve the identification of oil spills [53,66] and remove the radiometric sensor aging effects and radiometric discrepancy among sensors (i.e., Landsat TM and ETM+) [166]. Atmospheric correction softens the atmospheric effects by eliminating the influence of the atmospheric molecules and aerosol scattering [71] and improving the extraction of real surface parameters from satellite images (i.e., surface reflectance, emissivity, and surface temperature) [167]. This correction is considered in different oil spill studies [30,32,47,49,53,62,64,168].

Considering that oil spills can be monitored by different satellite-based or airborne imaging systems, geometric correction might need to be applied prior to image analysis if an image is to be compared with multitemporal and multisensory images or with existing vector data/maps. Image data should then be projected to a local or common projection system (i.e., Universal Transverse Mercator). Image enhancement, such as contrast enhancement, is applied to each image scene to enhance the oil slick visibility. Masking clouds, smoke, shadow, and land pixels can enhance the oil spill visualization and improve the discrimination of oil spills from the complex surrounding features [32,63].

3.2. SAR Images

Preprocessing of SAR data can generally be divided into four main steps, namely, radiometric calibration, geocoding, filtering, and masking. First, radiometric correction and calibration of SAR images are essential procedures to eliminate or reduce radiometric distortions and ensure that pixel values in SAR images are linked to the backscattering coefficient (sigma naught [measured in dB]) of the reflecting surface [169]. Thus, quantitative measurements (backscattered microwave energy from ground targets) restored from digital number values of image pixels and characteristics of an object in multitemporal SAR images acquired with different SAR sensors and modes can be compared [170,171].

The presence of geometrical distortions in SAR images (i.e., foreshortening, layover, and shadow) can minimize the use of SAR data and impede information extraction in various applications. Thus, geocoding of SAR data is required to minimize geometric distortions, and the location of any pixel in SAR imagery can be connected directly to the location on the ground [172]. In addition, the geocoding of SAR data facilitates the integration of geospatial data collected from different sources to improve monitoring and classification processes of oil spills. However, a high-resolution digital elevation model and additional knowledge, regarding orbit and sensor platforms, are needed for accurate terrain geocoding [173].

Unlike passive sensors, SAR images contain a certain degree of dark and light multiplicative noise known as speckle. The speckle noise is caused by the random interference of waves received by the sensor of many elementary reflectors within the ground resolution cell (or pixel) with a single resolution [174]. The noise may reduce the efficiency of information extraction techniques, human interpretation, automated scene analysis, and the analysis of multiple SAR observations [175]. Thus, speckle filtering is a crucial step in SAR images for oil spill classification systems. The optimal filtering technique should preserve the useful radiometric information and avoid the loss of scene features, such as local mean of backscatter, texture, linear features, edges, and point targets [176]. Various filter types with different kernel sizes were utilized by previous studies to reduce the speckle and enhance the SAR images for oil spill detection. Lee, enhanced Lee, Frost, Kuan, median, Lopez, boxcar, and non-local mean filters are some examples of the filters used in speckle filtering techniques. The most commonly used despeckling techniques for SAR images in the reviewed literature are the Lee [26,64,66,109,136,161] and enhanced Lee filters [112,149,154]. These filters are selected in oil spill studies due to their outstanding ability to minimize speckle noises while preserving edge sharpness and the important features in the SAR images. The final preprocessing step is masking out land and shorelines from SAR images. This process prevents the land from interfering with the detection of oil spills while reducing the computational intensity of the image [129]. In addition to the masking out of land and shorelines, weed beds and algae infestations can also be removed [15].

4. Feature Extraction

Feature extraction, a critical stage in oil spill detection systems, allows the extraction and input of a set of features to distinguish oil spills from lookalikes (natural phenomena, such as algae bloom, biogenic slicks, currents, and low-wind areas) and other targets on the water. The incorporation of features with reliable discriminatory power contributes to the improvement of classification accuracy in oil spill detection. Various studies have attempted to determine the optimal combination of different features for detecting and classifying oil spills [110,145,177–181]. However, the lack of systematic research on the extraction and combination of various sets of features (i.e., SAR polarimetric, textural, geometrical, and other features) and their influence on classification accuracies has generally contributed to the arbitrary selection of features as inputs to numerous classification systems [177,180]. The majority of reviewed studies explored the extraction of multiple features to detect oil spills from SAR and optical images in the last decade. The following section describes the widely used handcrafted (shallow) features in oil spill detection, while the automatic extraction of deep features is discussed in Section 5.2.

4.1. Feature Categories

Commonly used shallow features for identifying, detecting, and classifying oil spills can be categorized into the following five broad categories: statistical (i.e., mean, max, standard deviation, and ratios of backscattering coefficient values), geometric (i.e., area, perimeter, complexity, and shape factors and ratios), texture (i.e., derivatives of gray-level co-occurrence matrix [GLCM]), contextual (i.e., proximity to ships and oil platforms) [14,182,183], and SAR polarimetric (extracted from quad-, dual-, and single-polarimetric images) features. The detection of oil spills from optical images mainly focuses on the extraction of statistical [36,47,48,50–53,61,68,69], textural [46,184], and geometrical features [47]. Spectral, thermal, and textural properties are among the widely extracted features from optical images to differentiate oil spill and surface targets.

Considering that SAR data are extensively used in oil spill studies, various feature categories are extracted and utilized to differentiate oil spills and lookalikes. Commonly used feature categories and standard associated features for oil detection from SAR images are listed in Table 3. The frequency of adopting feature categories in differentiating oil spills and lookalikes from SAR images are shown in Figure 4.

Table 3. Common features extracted from SAR imagery.

Feature Category	Feature	Description	References
Geometric/ Shape	Area (A)	Area of an image object (in number of pixels)	[47,106,110,111,113–115,129, 136,138,141,142,145,163,177, 180,185–188]
	Perimeter (P)	perimeter of an image object (in number of pixels)	
	Complexity measure (C)	measure of the intricacy of an object geometrical shape $C = \frac{P^2}{A}$ or $C = \frac{P}{2\sqrt{\pi A}}$	
	Spreading (S)	S measures the ratio between an object's width and length	
	Shape factor	Measure of an image object border smoothness	[109–111,118,129,134,177, 180,186,188]
	Hu moment invariant [189]	Invariant moments used to characterize object patterns	[110,113,114,132,139,180, 190]
	Circularity	Measure of an image object compactness	[104,139,180,190,191]
	Perimeter to area ratio	Ratio of the perimeter to the area ($\frac{P}{A}$)	[106,110,118,177,180,188]
Statistical	Object standard deviation	Standard deviation of backscatter values an image object computed from SAR imagery	[106,109–111,113–115,134, 136,138,163,177,180,185, 188]
	Object mean value	Mean backscatter values of an image object	
	Background mean value	Mean backscatter values of a small region around the object	
	Background standard deviation	Standard deviation of backscatter values of a small region around the object	
	Max contrast	Difference between background mean value and the lowest backscatter value inside the object	
	Object power to mean ratio	Ratio between the standard deviation and the mean of an image object	
	Mean contrast ratio	Difference between background mean value and the mean backscatter value of the object	
	Gradient standard deviation	Standard deviation of the border gradient	[114,138,177,180,185,188]
	Mean border gradient	Mean value of the border gradient	
	Max gradient	Maximum value of the border gradient	
Texture	Contrast GLCM	GLCM contrast value computed from backscatter values of image objects	[111,113,114,129,135,136, 138,155,188,192–194]
	Homogeneity GLCM	GLCM homogeneity value computed for an image object	
	Entropy GLCM	GLCM entropy value computed for an image object	
	Correlation GLCM	GLCM correlation value computed for an image object	[110,113,129,155,192,195– 197]
	Dissimilarity GLCM	GLCM dissimilarity value computed for an image object	
	Variance GLCM	GLCM variance value computed for an image object	
	Energy GLCM	GLCM energy value computed for an image object	
	Mean GLCM	GLCM mean value computed for an image object	

Table 3. *Cont.*

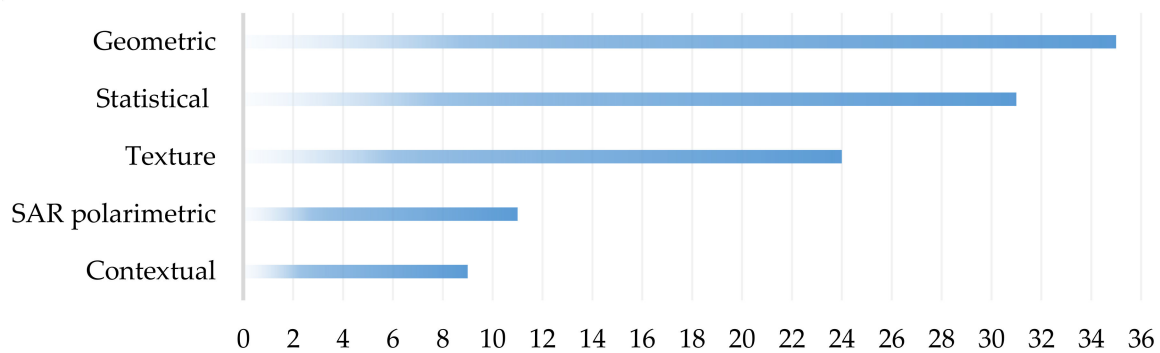| Feature Category	Feature	Description	References
SAR polarimetric features	Entropy	Polarimetric parameter used to measure the degree of randomness of the scattering mechanism	[103,128,198–200]
	Alpha angle	Polarimetric parameter used to characterize the scattering mechanism of the reflection	
	Degree of polarization	Physical quantity that is used to characterize the polarized light's polarization degree	
	Conformity coefficient	Evaluates if surface scattering is the dominant among all the scattering mechanisms [198], and it can discriminate surface, double-bounce, and volume scattering [201]	
	Correlation coefficient	Measure that reflects the averaged phase difference among scattering coefficients in co-polarized phases (i.e., HH, VV) [202]	[103,119,198,200,203]
	Anisotropy	Measures of the relative values of the second and third eigenvalues [204]	
	Pedestal height	Measure of the amount of the unpolarized backscattered energy [205]	
	Standard deviation of CPD (Co-Polarized phase Difference)	Standard deviation of CPD was introduced by [206] to differentiate oil and biogenic slicks	
Contextual	Number of neighboring targets in the same image	Number of adjacent targets to oil slicks in the same scene	[115,185]
	Distance to ship/rig	Distance from oil slick objects to ship, rig, and oil platforms in the surroundings	[110,142]
	Mean wind speed	Values of mean wind speed of image object	[132,139]

Figure 4. Number of studies that use each type of feature category.

Most oil spill studies combine various SAR features from different categories rather than rely on a single feature category only. Geometric and statistical features, followed by textural, SAR polarimetric, and contextual features, are frequently used to determine the contribution of each feature category. Several studies in which the feature selection process was conducted indicate that geometric features that are simple and easy to extract demonstrate higher discrimination power than other feature types [106,178]. For instance, spill released from a moving ship can appear in an SAR image as an elongated object of a particular width and length (Figure 3d). The ratio of the width to the length of the spillage could be used as a discriminative feature to differentiate between oil spills and their lookalikes. Area, perimeter, complexity, and spreading features are geometric features used in 39–49% of the total number of reviewed studies describing handcrafted features. Given that oil spills and their lookalikes can appear in diverse shapes under different and even similar environmental conditions, geometric features are usually combined with other feature categories. Object standard deviation, object mean value, background standard deviation, and maximum contrast, for instance, are common statistical features utilized in over 27–43% of the total number of reviewed studies discussing handcrafted features. The values and thresholds of the statistical features of an oil slick object extracted from optical or SAR imagery (i.e., mean, maximum, and standard deviation of a spectral band or backscattering coefficient), may vary from one data source/event to another owing to differences in oil characteristics, environmental conditions, sensor types, and specifications (i.e., wavelength, polarization, incidence angle). The texture of oil spills is continuous, smooth, and delicate, while that of their lookalikes is scattered, rough, and continuous [197]. Most textural features utilized in oil spill detection are based on GLCM. Contrast, homogeneity, and entropy are common GLCM-based features employed in over 23% of the total number of studies that use handcrafted features. However, GLCM features are computationally intensive compared with other feature types. Different SAR polarizations can help differentiate special features of the target and are considered in different studies to discriminate between oil spills and lookalikes. More than 21% of the studies rely on variations of SAR polarimetric features. Entropy (H), alpha angle (α), degree of polarization (DoP), and conformity coefficient are commonly used polarimetric features. Contextual features, which include information on the distance from the oil spill to a possible source, such as ships or oil rigs, are the least used features among the five categories [110,111,207]. Other contextual features may include weather data, such as wind speed, water depth, upwelling, atmospheric conditions (rain, dense fog, and aerosols), eddies, river inflow, location and direction of oil and gas pipelines, platforms, and vessels [64].

4.2. Feature Selection Techniques

Determining the optimal set of features for oil spill classification is based on the experience of researchers [180]. This step can be subjective and case-specific because the degree of importance of features may vary based on the data source, nature of the oil spill, complexity of surrounding surface features. The use of an excessive number of features in a classification scheme may result in the introduction of redundant features, increased processing time, and reduced classification

accuracy as well as influence the generalizability of the model [208,209]. Thus, feature selection (FS) techniques, which are dimensionality reduction strategies used to select relevant features and overcome these issues, are widely utilized as a critical step in classification tasks of remotely sensed data [210,211]. FS methods can typically be grouped into three main categories, namely, filter, wrapper, and embedded methods [212,213]. Filter methods utilize statistical measures (i.e., correlation coefficients and variance) to evaluate and rank features based on their degree of importance [213,214]. However, feature selection through filter-based methods does not involve the use of any classification algorithms. Different from the filter methods, the performance of a specific classification algorithm is used by wrapper methods to select relevant features that lead to the best classification result [215]. However, wrapper-based methods are computationally extensive and prone to overfitting, particularly when small training samples are used to train the adopted classification model [216]. Embedded methods are the trade-off strategies between the two methods that aim to optimize classification performance while decreasing the number of selected features [211,217]. The selection of the relevant subset is performed as part of the learning process of a classifier without an additional evaluation of the selected feature subset [218].

The utilization of FS techniques in oil spill detection systems is limited given the lack of systematic studies that focused on extracted features and their contribution to the classification results in oil spill detection and monitoring [180]. Only a few studies use various feature selection techniques to evaluate the effectiveness of different features and select optimal ones for oil spill detection. For instance, Mera et al. [180] employed filters and embedded methods, five feature selection methods, to choose a concise and relevant set of features for improving oil spill detection systems. Correlation-based feature selection, consistency-based filter, information gain, relief, and recursive feature elimination for support vector machines (SVMs) were applied on a 141-input vector comprising features from a collection of outstanding oil spill studies. The selection of relevant features expedited the feature extraction step without reducing classification accuracy. Chehresa et al. [110] used and evaluated eight different evolutionary algorithms (i.e., genetic algorithm, particle swarm optimization, and others) to select optimum feature subsets from 74 different types of features. High-frequency features with the highest number of repetitions among 30 independent repetitions of three evolutionary algorithms (genetic algorithm, fast, and classical evolutionary programming) were selected for classification as the optimum set of features.

5. Machine Learning

ML, a subset of artificial intelligence, refers to the ability of machines to learn and understand relationships between inputs and outputs from a full set of representative training samples, from which predictive and empirical classification models can be constructed without assuming any data distribution. ML can address specific issues even when the theoretical understanding of a particular problem remains inadequate regardless of the availability of a massive number of observations. Given the increasing availability of high-dimensional remotely sensed data and the complexity of pattern recognition tasks, ML techniques have been adopted for a full spectrum of the earth's observation applications such as oceanography [219–221], natural disasters [222–225] agriculture [226,227], land use [208,228,229], and environmental monitoring [230–232].

Various ML models have been proposed in the past decades to detect oil spills and distinguish between oil slicks and lookalikes, in which optical and SAR images are used to provide efficient monitoring solutions to mitigate the impact of oil spills. ML methods for oil spill detection are categorized in this review into traditional ML techniques and deep learning (DL) models. The succeeding subsections discuss and analyze various types of classical and advanced ML models for recognizing, identifying, and detecting oil spills obtained from remotely sensed data.

5.1. Traditional Machine Learning Techniques

The general framework of oil spill detection comprises the following four main steps: preprocessing of remotely sensed data, image segmentation for dark-spot identification, extraction of discriminative features, and classification of image pixels/objects to discriminate between oil spills and lookalikes. Sufficient and high-quality representative training samples and selected feature subsets demonstrated in Section 4.2 are used as inputs for developing classification models. ML models are developed to solve complex classification problems through recursive and iterative analysis of candidate solutions from given training samples and features without explicitly being programmed to do the task [233]. Various classification algorithms, such as artificial neural network (ANN) [50,52,141,146,163,199,207], SVM [145,180], decision tree (DT) [177], K-nearest neighbor [48,64], genetic algorithm [123,127,130], random forest (RF) [26], fuzzy logic [109,135,136,138], maximum likelihood [234], linear discriminant analysis [114,194], k-means [119], Mahalanobis distance [113], naïve Bayes [110], ensemble learning [46,115], Classification and Regression Trees (CART) [132], and others [38,51,140,142,235,236], have been used to classify oil spills and lookalikes. Widely used traditional ML classification model for oil detection from optical and SAR images are listed in Table 4. Figure 5 shows the frequency of common traditional ML algorithms in oil spill studies (a total of 79 studies). The following subsections provide a brief description of widely used traditional ML models in oil spill classification systems.

Table 4. Commonly used traditional ML models for oil spill detection.

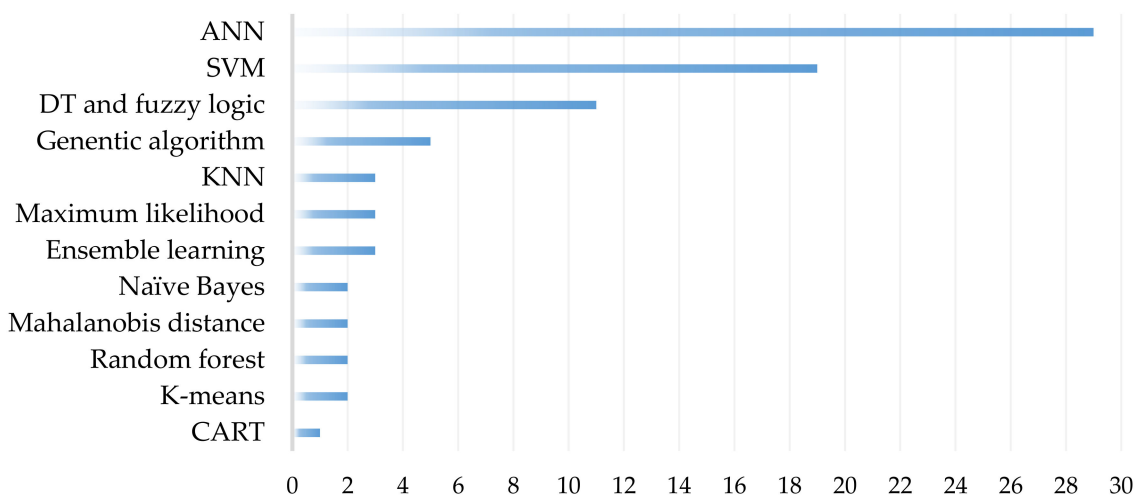| Classification	Sensor Type	Satellites	References
ANN	Optical	Landsat, DubaiSat-2, KOMPSAT-2, Landsat ETM+, GF-1	[52,53,63,68]
	SAR	ERS-1, ERS-2 and ENVSAT ASAR, RADARSAT-1, 2, ALOS PALSAR, TerraSAR-X, COSMO-SkyMed	[104,106,108,115,128,135,141,146,163,185–187,190,191,198,199,207,237–240]
SVM	Optical	MODIS (Band 1 and 2), AVIRIS, HJ-1 and Landsat ETM+, GF-1	[32,46,53,192]
	SAR	TerraSAR-X, ENVISAT ASAR, UAVSAR, RADARSAT-1, 2, RISAT-1, Shipborne radar	[21,27,114,115,121,145,154,180,185,192,198,241,242]
DT/fuzzy logic/rule-based	Optical	MODIS (Band 1 and 2), IKONOS, Quickbird, RapidEye, WorldView2, Landsat TM	[36,47,69]
	SAR	ERS-2, ENVSAT ASAR, TerraSAR-X, RADARSAT	[36,109,129,134–136,138,147,177]
KNN	Optical	LANDSAT-8, MODIS (Terra and Aqua)	[48,64]
	SAR	ENVISAT, ERS-1/2, TerraSAR-X, RADARSAT-1, SENTINEL-1,ERS-1,2	[64,112]
Genetic algorithm	SAR	RADARSAT-2	[123,124,127,130]
Extreme learning	SAR	ENVISAT ASAR	[196]
Ensemble learning	Optical	MODIS (Band 1 and 2)	[46]
	SAR	RADARSAT-1	[115]
Maximum likelihood	SAR	RADARSAT-2	[198,234]
Naïve Bayes	SAR	ERS-1, ERS-2, ENVISAT and RADARSAT-2	[110]
Mahalanobis distance	SAR	ERS-1, 2	[113]
Random forest	SAR	Radarsat-2 and UAVSAR	[26]
Cart	SAR	ENVSAT ASAR	[132]
K-means	SAR	RADARSAT-2	[26,119]
Others	Optical	MODIS (Band 1 and 2), Landsat 8, GF-1, and HJ-1	[38,51]
	SAR	ERS-1, 2, RADARSAT-1, ENVISAT ASAR, Sentinel-1, PALSAR and TerraSAR-X	[111,115,137,140,142,162,185,191,236,243]

Figure 5. Frequency of traditional classification algorithms in oil spill studies.

5.1.1. Artificial Neural Network

Inspired by the functionality of the biological nervous system, ANNs are computing systems that entail a set of algorithms working together to simulate the structure and functions of the human brain. The relationship between input parameters and their output responses are derived using highly interconnected processing units (artificial neurons), a training or learning algorithm, and activation functions [244,245]. The basic ANN topological structure consists of three layers, namely, input, hidden (may be more than one), and output layers. The training procedure of ANNs involves the determination and adjustment of associated weights on connections in three main stages; namely, the feedforward of input data, calculation of the associated error between the input and output, and adjustment of weights [246]. Upon the completion of the training and accuracy evaluation phases, the developed neural network model can predict the presence and absence of oil spills in unseen data with similar feature characteristics.

Feedforward ANNs with backpropagation optimization algorithm are widely used ML algorithms for oil spill classification and account for almost 27% of the reviewed literature in this work (a total of 29 studies). A key challenge in the utilization of ANN for oil spill classification is the determination of optimal combinations of ANN hyperparameters, such as the number of hidden units, batch size, training iterations, learning rate, and momentum, because poor choices may negatively impact its accuracy and computing performance. A trial-and-error strategy is commonly used to determine and evaluate the appropriateness of multiple combination sets of these parameters. For instance, Park et al. [52] implemented ANN architecture to classify oil spills from optical images with the following settings: 1000 epochs, learning rate of 0.01, and hidden layer of eight neurons. Chen et al. [103] implemented ANN to classify oil spills from SAR images with the following parameter settings: 100 epochs, learning rate of 1.0, and two hidden layers of eight and six neurons. Reported accuracies of ANN in oil spill studies range from 72% to 99%.

5.1.2. Support Vector Machine

SVM [247], a nonparametric supervised ML technique based on the principle of structural risk minimization from statistical learning theory, has been successfully used in a wide range of remote sensing applications. The popularity of adopting SVM in the field of oil spill classification (almost 17% of the reviewed literature use SVM) can be attributed to its ability in handling high-dimensional feature space and achieving satisfactory classification results with a limited number of training samples. SVMs specifically focus on samples that are adjacent to borders between classes in the feature space, which are called support vectors; these SVMs aim to determine the location of a separating hyperplane (decision boundary), which produces the optimal separation of classes to minimize misclassifications

and achieve satisfactory generalization capability [248]. Earlier versions of SVM were originally developed for binary classification by identifying the optimal hyperplane in linearly separable cases; kernel tricks were then introduced to address this limitation by mapping the data into a high-dimensional feature space and constructing an optimized separating hyperplane that deals with nonlinear decision surfaces [249–251]. Various kernel functions, including linear, polynomial, sigmoid, and radial basis function (RBF) kernels, are used to reduce the computational cost of dealing with high-dimensional feature spaces [248]. RBF [22,112,114,115,155,185,198] and polynomial kernel [194] are commonly used kernels in oil spill studies. However, the selection of the appropriate kernel type and its parameter configuration should be considered when adopting SVM for oil spill classification. Reported accuracies of SVM in oil spill studies range from 71% to 97%.

5.1.3. Decision Tree

DT is a simple and straightforward nonparametric ML technique classifier that recursively divides the input dataset into branches of data subsets; each subset is described by a set of features, thresholds, and a class label [252,253]. Compared with ANN and SVM, DT can be trained and executed rapidly and analysts can easily interpret the output of the model. DT is widely used to aid the development of ruleset for the classification of remotely sensed data using object-based classification approach due to its ability to handle nonlinear relationships between features and feature values from different scales or range of values and classes. Topouzelis and Psyllos [177] highlighted that tree size plays a significant role, especially because the tree deals with two classes, namely, oil spills and lookalikes. A tree size that is neither excessively large nor excessively small will correctly represent feature vectors. Moreover, tree classifiers are very sensitive to small changes that occur in the training dataset; thus, the careful development of a training dataset is required to distinguish between oil spills and lookalikes successfully [129,177]. Compared with other traditional ML classifiers, DTs and fuzzy logic have been adopted in fewer oil spill studies (10% of the reviewed studies). The reported accuracies of DT and fuzzy logic in oil spill studies range from 80% to 96%.

Differences in oil spill classification results reported in the literature are likely due to various factors affecting the performance of ML classifiers, including variations in the data source, data preprocessing techniques, training sample size, number and quality of selected features, and choice of classification algorithms and their parameter settings. A study is considered case-specific when the performance of ML models for oil spill detection is compared without unifying all possible influencing factors. Thus, comparing the performance of traditional ML algorithms in terms of their accuracy for oil spill detection using different datasets is problematic [104]. Several studies have compared the performance of numerous traditional ML models for oil spill detection using the same data source [115,139,198]. Zhang et al. [198], for example, compared three widely used supervised classifiers (i.e., ANN, SVM, ML) for oil spill classification using complete and compact polarimetric SAR images. SVM, followed by ANN, outperformed ML when sufficient polarimetric information (i.e., quad polarization) was obtained. Mera et al. [139] studied the performance of 428 classifiers of 41 families, including ensembles, SVM, ANN, Bayesian, DT, RF, and many others, for oil spill detection using 47 ENVISAT ASAR images. The group's experiments showed that the best classification accuracies are achieved by the rotation forest ensemble of multilayer perceptron base classifiers. Yang et al. [53] evaluated the performance of ANN, SVM, MD, and ML for oil spill extraction from GF-1 images using an object-based approach. The results of single classifiers demonstrated that ANN and SVM are superior to other classifiers, while the results of multiple classifiers (decision level fusion) revealed that the classification accuracy of SVM-ANN is slightly higher than that of ANN.

5.2. Deep Learning Techniques

Inspired by the structure and function of the human brain, DL algorithms are a series of distinct deep neural networks (DNNs) that automatically learn complex discriminative features from considerably large amounts of data in a hierarchical manner to extract information through

multiple high-level layers of abstractions [254,255], demonstrate remarkable capabilities, and achieve remarkable success in various fields of remote sensing and geoscience. Unlike traditional ML approaches, DL is completely data-driven, in which natural relationships between input and output data are automatically constructed and feature representation characteristics are solely learned from the data [256]. Therefore, the feature extraction step dependent on expert knowledge in constructing handcrafted features prior to the classification phase of the oil spill is eliminated. Various DL models exhibited outstanding performance in detecting oil spills from SAR and optical images through the automatic extraction of discriminative learned features to distinguish between oil spills and lookalikes. Moreover, the generalization ability of these models can address the case-specific nature of traditional techniques. The number of oil spill-related studies that adopted DL models has increased since 2017. These models were used to perform diverse tasks, such as oil spill detection and recognition [257,258], image patch-based classification [83,103,197], and semantic segmentation [259–265]. Depending on the neural network architecture, DL models can vary in terms of their architecture, components, and tasks, which can consist of convolution layers, activation functions, pooling layers, fully connected layers, memory cells, gates, encoder/decoder, and others [266]. Commonly used DL models include convolutional neural network (CNN), autoencoder (AE), recurrent neural network (RNN), deep belief network (DBN), and generative adversarial network (GAN). Table 5 lists the different DL models adopted in oil spill studies for performing various tasks. The following subsections review some of these models in the context of oil spill identification and detection.

5.2.1. Convolutional Neural Network

CNNs [267] are widely used DL techniques in image recognition due to their weight-sharing network structure, which allows the direct feed of images into the deep network [258]. The underlying architecture of CNNs consists of a set of convolutional layers, activation functions, pooling layers, and fully connected layers (Figure 6). CNNs are typical feedforward DNN architectures that can learn highly abstract features from original representations of images through a set of convolutions and mathematical operations, which preserve the spatial relationship among pixels and reduce the effective number of learning parameters [268].
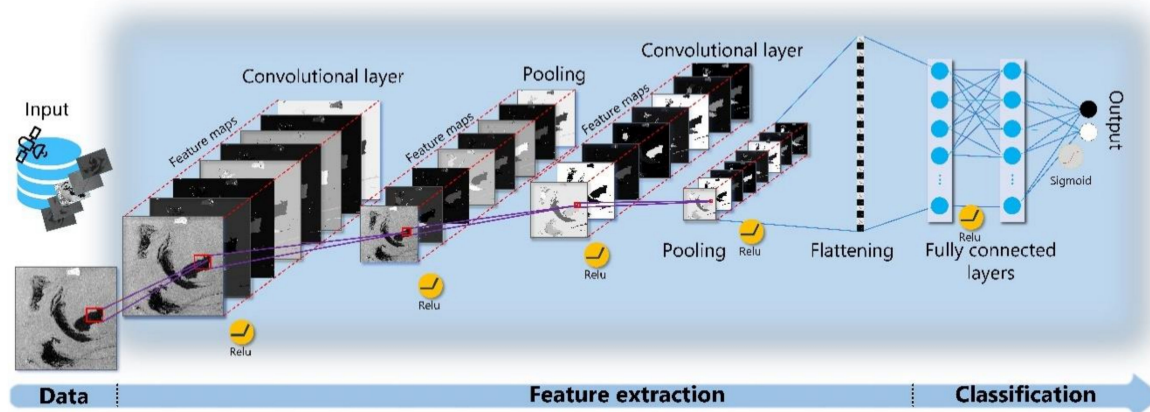

Figure 6. General CNN framework.

Convolutional layers are used to perform feature extraction by utilizing several learnable convolutional kernels or filters on a small area of the input data based on the kernel size. The result of each convolutional function undergoes nonlinear transformation via an activation function (e.g., rectified linear unit, sigmoid, hyperbolic tangent, and softmax) to obtain nonlinear convolved features or so-called feature maps (i.e., multiple maps of neurons) and increase the nonlinear fitting capability of CNN.

Table 5. Commonly used DL models for oil spill detection.

DL Models	DL Task	Data	Architecture	Input Data Size	Labelled Data	Reference
CNN	Patch-based classification	ERS-2	DenseNet	224 × 224	A total of 86 oil film samples and 62 oil film samples.	[258]
		ERS-2	VGG-19	224 × 224	A total of 87 and 63 oil slick and look-alike oil slick samples, respectively.	[269]
		ENVISAT, ERS-1,2, COSMO Sky-Med	VGG-16	64 × 64	A total of 4843 and 18,925 oil slick and look-alike samples, respectively.	[270]
		RADARSAT-2	Two convolutional and pooling layers	28 × 28	A total of 2100 crude oil, 2100 plant oil, and 2100 oil emulsion samples	[197]
		AVIRIS	1D CNN	-	A total of 469,567 and 42,676 samples were selected for training and testing, respectively.	[22]
		RADARSAT-2	Five-layer CNN architecture + SVM	15 × 15	A total of 26,000 and 6500 samples were used for training and testing, respectively.	[271]
	Object detection	SLAR	Two-stage CNN	50 or 28 pixels per side (with an overlap of 25 and 14 pixels)	A total of 23 SLAR images (512,566 samples)	[272]
		Unmanned aerial vehicle (RGB)	Faster R-CNN	-	A total of 1096 and 958 images were used for training and testing, respectively.	[273]
	Semantic Segmentation	Sentinel-1	DeepLabv3+	321 × 321 pixels	A total of 1002 and 110 images were used for training and testing, respectively.	[260]
		Radarsat-2	SegNet	256 × 256 pixels	A total of 3600 and 600 samples were used for training and testing, respectively.	[262]
		ENVISAT and Sentinel-1	Fully CNNs	128 × 128 pixels; 2048 × 2048 pixels	A total of 630 images were used for the training process.	[265]
		QuickBird, Worldview, and Google Earth	Deeplab + fully connected conditional random field	-	Approximately 60%, 20%, and 20% of the 8400 images were used for training, testing, and validation, respectively.	[259]
		Radarsat-2 and SIR-C/X-SAR	Encoder–decoder CNN and simple linear iterative clustering superpixel	48 × 48 pixels	A total of 356 and 122 samples were used for training and testing, respectively.	[261]
		Sentinel-1	DeepLab	1250 × 650 pixels	The training and testing sets consist of 771 and 110 images, respectively	[274]
		Landsat-8 and Landsat-7	FCN-GoogLeNet and FCN-ResNet models	-	Yantai and Bohai bay datasets	[275]
		Sentinel-1	DeepLab	1252 × 609 pixels	The training and testing sets consist of 571 and 106 images, respectively.	[264]
		Sentinel-1	fully convolutional network based on U-net	160 × 160 pixels	Three sets of data were used, and each set was divided into training, testing, and validation patches.	[276]
		Sentinel-1	Mask R-CNN	1024 × 1024	A total of 2882 images were labelled for training and validation.	[277]

Table 5. *Cont.*

DL Models	DL Task	Data	Architecture	Input Data Size	Labelled Data	Reference
AEs	Classification	AVIRIS	Stacked AE	-	A total of 1500 and 315 pixels were used for training and validation, respectively	[83]
		RADARSAT-2	Stacked AE and DBN	20×20	A total of 24,000 data samples	[103]
	Segmentation	SLAR	Selectional AE, and very deep Residual Encoder-Decoder Networks	256×256 384×384	A dataset with 28 flight sequences	[278]
		SLAR	Long Short-Term Memory Selectional AE	-	A dataset composed of 51 flight sequences	[263]
DBN	Classification	Radarsat-2	DBN with Restricted Boltzmann Machine	32×32	A total of 600 and 300 samples were used for training and testing, respectively.	[195]
RNN	Classification	SLAR	MLPs, Vanilla RNN, LSTM networks, Bidirectional LSTM networks	-	A total of 12 SLAR records	[279]
GANs	Segmentation	ERS-1, 2, ENVISAT ASAR	Adversarial f-divergence	256×256	-	[280]

Feature maps and the input image have similar output sizes. The dimensionality of feature maps is reduced by subsequent pooling layers (e.g., max and average pooling layers) to acquire features but insensitive to precise locations of targets, thereby ensuring that effective features can still be learned by the network [281]. Therefore, feature maps are generally downsampled by half using pooling layers to increase the abstraction of extracted features and reduce the input dimensionality of feature maps while maintaining the depth to minimize the computational power and circumvent overfitting by cutting the number of learnable parameters [282]. Additional pooling operations, such as stochastic [283], spatial pyramid [284,285], and atrous spatial pyramid pooling [286], are also used by several studies. Feature maps extracted through convolutional and pooling layers are transferred into a one-dimensional vector by flattening the layer that connects outputs of CNN layers with fully connected layers.

A fully connected layer, which is mounted at the top of the architecture, is composed of multiple hidden layers and computes the score of each class using convolved features from former layers. The output of fully connected layers is known as the classification layer. The classification results are derived through activation functions, such as sigmoid (for binary classification, which involves indicating the existence or absence of oil spill) and softmax functions (for assigning the probability that belongs to multiple classes, such as oil spills, ships, and lookalikes). Forward and backpropagation are two primary processes for training and learning weights of parameters between the input and output of the network. Forward propagation involves the transmission of characteristic information and optimization of weights of learnable parameters of the network through iterative backpropagation processes to minimize the value of a defined cost function [261].

CNNs are widely used as DL models in oil spill detection due to their outstanding performance and versatility in object detection (e.g., a label and a bounding box are produced from given image tiles to show the oil spill location in each image), image classification (e.g., a label from the given image tiles is used to indicate the content of each tile), and semantic segmentation (e.g., a segmentation or probability map is created for predefined classes from given image tiles). Different tasks and architectures of CNN for oil spill detection are discussed in the following subsections.

Patch-Based Image Classification

Patch-based CNN models are constructed based on equally spaced selected tiles (patches) from remotely sensed images, and each tile corresponds to one class label. The CNN model can be designed to produce a probability map of each input patch label for every tile to indicate the probability of the presence or absence of an oil spill in an image tile. The determination of the optimum size of the input patch for CNN classification can be considered a critical factor. For example, the selection of a small input image patch size may hinder the CNN model from learning discriminative features, whereas the selection of a large one adds computational burden on the network and increases the overall processing time [197]. Various CNN structures were used to classify oil spills from patches of remotely sensed data. Yaohua et al. [258] presented a densely connected CNN network structure based on DenseNet to recognize oil slicks from lookalikes in ERS-2 SAR data of the China Sea. A total of 148 images that represent 86 oil slick and 62 lookalike samples were selected from ERS-2 data to develop the DenseNet model. Considering the limited number of samples, the mixing of the oil and oil-like slicks was ignored. Zeng and Wang [270] developed a deep oil spill CNN based on the VGG-16 model by designing and adjusting the CNN architecture and hyperparameters using a large dataset comprising SAR dark patches. A total of 4843 oil slick and 18,925 lookalike samples were generated through manual labeling and data augmentation techniques and subsequently utilized to develop the model.

The incorporation of parametric SAR and optical features to improve the performance of patch-based classification was investigated by different researchers. For instance, Guo et al. [197] utilized SAR polarimetric features (i.e., entropy, alpha, and single-bounce eigenvalue relative difference) extracted from C-band SAR data to develop a CNN that can differentiate crude oil, plant oil,

and oil emulsion. The CNN model was trained using 5400 samples and achieved a recognition rate of 91.33%. Song et al. [271] extracted deep features of SAR polarimetric data using a CNN model, which was accompanied by dimensionality reduction through principal component analysis and followed by an SVM classifier with radial basis kernel to identify oil spills. Liu et al. [22] extracted spectral indices from AVIRIS hyperspectral images and used a one-dimensional CNN to mine spectral feature information deeply and extract oil films automatically. The CNN model outperformed traditional ML models, such as SVM and RF.

Object Detection

CNN-based object detection techniques contain a two-stage mechanism, where shared discriminative feature maps are initially extracted using CNNs and candidate region proposals are subsequently generated to localize object(s) within an image and output corresponding categories [287]. Various generic object detection techniques based on deep CNNs (DCNNs) can detect, localize, and predict the label of the target to deliver state-of-the-art detection performance [288]. Faster region-CNN (R-CNN) [289], mask region-based CNN (mask R-CNN) [290], you only look once [291], and single-shot multibox detector [292] are examples of models that achieve satisfactory performance in object detection. Previous studies adopted DCNNs to perform object detection of targets in water surfaces for detecting ships [293–296]. Few studies focused on investigating oil spills. Nieto-Hidalgo et al. [272] presented a system for detecting ships and oil spills from SLAR images using a two-stage CNN. Huang et al. [273] applied faster R-CNN to locate and classify the spill of floating hazardous and noxious substances from optical images. Jiao et al. [257] constructed and optimized a DCNN model using faster R-CNN on the basis of a pretrained network on ImageNet to detect oil spills on lands using unmanned aerial vehicle-based data. The results showed that the cost of inspecting oil spills reduces by 57.2% compared with the cost incurred in the traditional manual inspection process.

Semantic and Instance Segmentation

Image segmentation, based on pixel-wise classification using DNNs, can be categorized into semantic and instance segmentation [297]. Semantic segmentation, a widely used concept in computer vision that has the same meaning as per-pixel classification used among remote sensing communities, conducts pixel-level classification to assign a category to every pixel in a remotely sensed image. Sea surface areas, ships, and oil spill areas can be accurately classified through semantic segmentation, which can also provide comprehensive knowledge of an image [259]. Unlike patch-based and object detection methods, semantic segmentation accurately delineates the boundary and position of the target of interest and renders it suitable for processing remote sensing images [298]. Numerous semantic segmentation models, including fully connected network [299], fully connected DenseNet [300], U-Net [301], pyramid scene parsing network [302], SegNet [303], RefineNet [304], pyramid attention network [305], DeepLab series [286,306], and discriminative feature network [307], were proposed and adopted in the field of computer vision.

By comparison, instance segmentation models are hybrid approaches that incorporate semantic segmentation and object detection algorithms to localize objects and deliver their per-pixel classification simultaneously. Yekeen et al. [277] recently developed an instance segmentation mask R-CNN model to localize and segment oil spills and different elements within the surrounding areas of oil spill incidents. The developed model combines the feature pyramid network architecture (used for extraction features at different scales) and transfer learning approach through the pretrained ResNet 101 on COCO datasets. The performance of the mask R-CNN and approaches that utilized a set of classical ML [106,109,139,180,185,308] and DL models [260,270,278] in other studies was compared. The reported results indicated that mask R-CNN outperformed other CNN models in the literature. However, a comprehensive evaluation on the performance of diverse CNNs and the influence of various factors, such as the number of samples, hyperparameter settings, optimization algorithms, and transfer learning on the performance of oil spill detection are lacking.

5.2.2. Autoencoder

Hinton and Zemel [309] introduced AE, which is a feedforward neural network trained to transform its inputs into outputs. This transformation can be achieved through the utilization of an encoder–decoder structure in an unsupervised manner. Although the encoding step transforms characteristics of input data into a low-dimensional space, the decoder step takes the top extracted representative characteristics as the input and attempts to reconstruct such an input. AE aims to set target values to be as close to the original input as possible [310]. This outcome is achieved by adjusting parameters of the network and consistently comparing the input and output through backpropagation until a minimal amount of discrepancies between the input and output is achieved. Several AE architectures, such as multilayer, stacked (SAE), sparse, denoising, adversarial, variational, convolutional, and vanilla AEs, have been proposed to solve different types of problems. Additional information on different types of AEs are discussed in [310,311].

Motivated by the lack of studies using DL in the feature optimization for oil spill detection, Chen et al. [103] utilized SAEs and DBNs to reduce the dimensionality, optimized SAR polarimetric features in an unsupervised manner, and used them as input in a supervised classification procedure to classify marine oil spills and biogenic lookalikes. SAE and DBNs successfully boosted and achieved more accurate classification result using a given limited number of samples compared with classical algorithms. Liu et al. [83] used hyperspectral data and proposed a spatial–spectral jointed SAE (SSAE) to extract and classify oil slicks on the sea surface. The performance of the proposed SSAE was compared with the results of SAE, SVM, and BPNN algorithms (multilayer feedforward network trained according to error backpropagation); the results indicated that the proposed model remarkably outperformed other models. Two recent studies [263,278] adopted two different AE architectures to segment oil spills from an airborne SLAR dataset. Gallego et al. [278] utilized SelAE with very deep residual encoder–decoder networks to segment and identify oil spills from the SLAR data set. Bazine et al. [263] developed a selectional AE with convolutional long short-term memory to segment oil spills and other maritime classes (ship, lookalike, coast, central noise, lateral turns, and water) from scanlines of SLAR airborne images simultaneously.

5.2.3. Other Deep Learning Models

CNNs, followed by AEs, are commonly used DL models for identifying oil spills from remotely sensed data; however, only a few studies have adopted other DL models, such as DBN, RNN, and generative adversarial network (GAN). Chen and Guo [195] proposed a DBN model to distinguish oil spills, lookalikes, and water in three SAR images from a small sample space database. Chen et al. [103] analyzed and compared the performance of SAE, DBN, and several classical algorithms to identify the presence of oil spills from a limited number of samples. The performance of both DBN and SAE achieved better performance than classical ML algorithms.

A DL model based on RNN, which is a network where connections form directed cycles designed for processing sequential data, was presented in [279] to identify candidate oil spills from SLAR scanned sequences rapidly. The RNN model achieved better performance compared with a multilayer perceptron neural network. An encoder–decoder structure-based adversarial learning of f-divergence minimization function was introduced in [280] to segment oil spills from SAR images automatically. Different forms of deep networks are structured to produce a segmented instance of the input image via a generator initially and minimize the f-divergence between ground truth and the generated segmentation result by a regressor. One advantage of this model is the ability to segment irregular oil spills even in extremely noisy conditions given the comprehensiveness of the f-divergence and its capability to address rigorous situations. However, this method is limited to one-class segmentation (i.e., oil spill) without completely maximizing the pixel-wise classification delivered by semantic segmentation methods.

6. Discussion and Conclusions

Oil spills on seas and oceans, a major source of maritime and ocean pollution due to anthropogenic activities and the growing demand for oil and maritime transport capacity, pose a deleterious effect on aquatic and wildlife, maritime tourism, aquaculture, and commerce. Constant monitoring and early intervention of oil spills are crucial and urgently needed to minimize their environmental impacts and economies of coastal states. The capability of monitoring, detecting, and managing oil spills remotely is vital due to persistent dangers posed to marine biodiversity, wildlife, and habitats. The past decade has shown remarkable advances in the field of oil spill detection due to the increasing availability of remotely sensed data, growth of computation power, availability of cloud computing infrastructure, and development and adoption of state-of-the-art ML algorithms.

Satellite and airborne remote sensing techniques have been extensively used to detect, monitor, characterize, and estimate the thickness of oil spills. These techniques include the use of visible and infrared multispectral, hyperspectral, thermal, microwave, and laser fluorosensors. Oils in seas and oceans exhibit different characteristics in various wavelengths across the spectrum. Figure 2a,b and Figure 3a,b show the differences in the appearance and information of an oil spillage event captured by Sentinel multispectral and SAR sensors near the coast of Mauritius and Kuwait. Microwave satellite-based SAR data are widely used data source compared with other sources for oil spill detection due to their sunlight independence, cloud coverage, and availability in all types of weather conditions. The use of satellite-based multispectral data is increasing, owing to their growing availability, synoptic coverage, and unique spectral characteristics. These optical features assist the differentiation between oil spills and lookalikes. The utilization of other sensors—such as ultraviolet and laser fluorosensors—in oil spill detection systems remains limited. Each remote sensing technique has its own advantages and shortcomings (i.e., data cloud contamination and presence of shadow in optical data). Leveraging multisource data can provide valuable information, fill the temporal gap, and enable timely and effective oil spill monitoring and management.

Similarities between oil spills and other natural or manmade regions (lookalikes) in optical and SAR images affect the accuracy of oil spill detection systems. The inclusion and combinations of various feature categories (i.e., statistical, geometric, texture, and SAR polarimetric features) with robust discriminatory power help discriminate between oil spills and counterparts and improve the accuracy of oil spill classification models. A wide range of oil spill studies rely on the manual extraction and incorporation of different feature categories based on analysts' experience. However, few studies utilize feature selection techniques (i.e., filter and embedded methods) to select remarkable features with high discriminative power for improving the classification accuracy and generalization ability of oil spill classification systems. Considerable efforts should be exerted in evaluating the efficiency of extracted features from optical and SAR images and their contribution to the classification results in oil spill classification systems.

The acquisition and selection of adequate and high-quality representative training samples (ground truth samples) are critical factors that control the performance of classification algorithms. Maxwell et al. [312] argued that information regarding the minimum number of samples required by ML classifiers is still unknown. Ample high-quality representative training samples of oil spills and lookalikes are essential in selecting discriminatory features and developing accurate and reliable classification systems. The collection of accurately labeled oil spill samples is a challenging task that requires meticulous attention considering similarities between natural phenomena known as lookalikes, which produce a signal similar to oil spills. In some circumstances, a human expert may have difficulty in determining whether dark regions on the image are oil spills or lookalikes. These uncertainties may result in the introduction of some false positive and negative errors in the process.

Moreover, oil spill incidents spatially cover a small percentage of the entire data and training datasets are collected from multiple time-series images acquired at different locations with varied oil characteristics; thus, expected dissimilarities between samples may ultimately affect the training and generalization capability of the developed classification approach [14,313]. The scarcity of in situ

oil spill data, uncertainties encountered during the selection of oil spill samples from SAR images, presence of class imbalance between oil spills, and lookalikes are some challenges that may affect the development of accurate ML classification models with high generalization capabilities.

Various classical and advanced ML models have been adopted in the past decade for oil spill detection and classification. Different classical ML models were used in 72% of the reviewed studies. The generic framework for developing automatic oil spill detection systems from SAR images using traditional ML models may include preprocessing of remotely sensed data, identification/segmentation of dark spots, extraction of discriminative features, and classification of image pixels/objects with various classification models. ANN, SVM, DT and fuzzy logic are among the widely used classical ML models for oil spill detection. However, the literature presented varied classification results for these methods. A thorough comparison between various classical ML classifiers under the same data source, preprocessing techniques, size of training samples, number and quality of selected features, and choice of parameter settings of classification algorithms is ideal.

The potential for overfitting occurs when a classifier achieves high accuracy on a dataset while failing to generalize well on unseen data. This condition is a common concern when ML models are developed with limited training samples. Thus, evaluating the performance of a classifier on a new dataset that is not used during the training phase is imperative.

Versatile DL models (accounting for 28% of the reviewed literature) recently demonstrated remarkable success in detecting oil spills from SAR and optical images by automatically extracting discriminative features to differentiate among oil spills, lookalikes, and other targets. The generalization capability of DL models addresses the case-specific nature of classical ML techniques. DL algorithms with different architectures were used to perform diverse tasks, including object detection, patch-based classification, and semantic and instance segmentation of oil spills. CNNs, AEs, RNNs, DBNs, and GANs are commonly used DL models for oil spill classification. CNNs and AEs are utilized more than other DL models for oil spill detection and segmentation. Although the adoption of various DL models and architectures for the identification and detection of oil spills/slicks has increased and achieved promising results, the following challenges still exist:

- The process of preparing considerable amounts of labeled data to train a DL model is a laborious and time-consuming task. Given the similarities between oil spills and lookalikes (i.e., dark spots created by natural phenomena, such as regions with low wind speed, wave shadows, and biogenic slicks/films) in SAR images, the process of defining training samples is challenging and susceptible to human errors.
- The limitation or absence of accessible open-source annotated datasets compromise oil spill/slick images collected from various multisensory sources at different locations with diverse environmental variations and oil characteristics.
- The fine-tuning of DL model hyperparameters (i.e., number of filters, batch size, learning rate, momentum, weight decay, and others) requires an extensive trial-and-error experimentation to determine optimum configurations of parameters. A wide variety of hyperparameters should be considered and investigated for practical use.
- A thorough investigation on the performance and generalizability of DL models to detect the presence of oil spills from unseen datasets collected from different environments in the literature is lacking.
- A detailed classification of oil spills/slicks—including oil type, thickness, or other chemical properties—via DL models is lacking in the literature.

Considering the continuous development in remote sensing technologies, cloud computing services, and computer vision along with the increasing accessibility of publicly annotated remotely sensed data (i.e., SpaceNet [314], CleanSeaNet service [315],), the aforementioned challenges can be mitigated in the future. The development of real-time monitoring and detection systems of oil spills with unmanned

aerial vehicles (UAVs) is inevitable due to the miniaturization of sensor technologies and advances in UAV technology.

References

1. Li, P.; Cai, Q.; Lin, W.; Chen, B.; Zhang, B. Offshore oil spill response practices and emerging challenges. *Mar. Pollut. Bull.* **2016**, *110*, 6–27. [CrossRef] [PubMed]

2. De Oliveira, O.M.C.; Antônio, A.F.; Cerqueira, J.R.; Soares, S.A.R.; Garcia, K.S.; Filho, A.P.; Rosa, M.d.L.d.S.; Suzart, C.M.; Pinheiro, L.d.L. Environmental disaster in the northeast coast of Brazil: Forensic geochemistry in the identification of the source of the oily material. *Mar. Pollut. Bull.* **2020**, *160*, 111597. [CrossRef] [PubMed]

3. Chang, S.E.; Stone, J.; Demes, K.; Piscitelli, M. Consequences of oil spills: A review and framework for informing planning. *Ecol. Soc.* **2014**, *19*, 26. [CrossRef]

4. Chen, J.; Zhang, W.; Wan, Z.; Li, S.; Huang, T.; Fei, Y. Oil spills from global tankers: Status review and future governance. *J. Clean. Prod.* **2019**, *227*, 20–32. [CrossRef]

5. ITOPF. The International Tanker Owners Pollution Federation Limited Oil Tanker Spill Statistics. 2020. Available online: http://www.itopf.com/knowledge-resources/data-statistics/statistics/ (accessed on 30 September 2020).

6. Gokce Cicek Ceyhun, A. The impact of shipping accidents on marine environment: A study of turkish seas. *Eur. Sci. J.* **2014**, *10*, 1857–7881.

7. Ober, H.K. Effects of Oil Spills on Marine and Coastal Wildlife. *Inst. Food Agric. Sci.* **2010**, 1–4.

8. Mishra, A.K.; Kumar, G.S. Weathering of oil spill: Modeling and analysis. *Aquat. Procedia* **2015**, *4*, 435–442. [CrossRef]

9. Leifer, I.; Lehr, W.J.; Simecek-Beatty, D.; Bradley, E.; Clark, R.; Dennison, P.; Hu, Y.; Matheson, S.; Jones, C.E.; Holt, B.; et al. State of the art satellite and airborne marine oil spill remote sensing: Application to the BP deepwater horizon oil spill. *Remote Sens. Environ.* **2012**, *124*, 185–209. [CrossRef]

10. Sadek, M.E.; Seheimy, A.E.; El-Tokhy, T.T.; Allah, M.A. Management process of oil spill in water plants. *J. Pollut. Eff. Control* **2017**, *5*. [CrossRef]

11. Ivshina, I.B.; Kuyukina, M.S.; Krivoruchko, A.V.; Elkin, A.A.; Makarov, S.O.; Cunningham, C.J.; Peshkur, T.A.; Atlas, R.M.; Philp, J.C. Oil spill problems and sustainable response strategies through new technologies. *Environ. Sci. Process. Impacts* **2015**, *17*, 1201–1219. [CrossRef]

12. Michel, J.; Fingas, M. Oil spills: Causes, consequences, prevention, and countermeasures. In *Fossil Fuels: Current Status and Future Directions*; World Scientific: Singapore, 2016; pp. 159–201. ISBN 9789814699983.

13. Fingas, M.; Brown, C.E. Oil Spill Remote Sensing: A Review. In *Oil Spill Science and Technology*; Elsevier: Amsterdam, The Netherlands, 2011; pp. 111–169. ISBN 9781856179430.

14. Brekke, C.; Solberg, A.H.S. Oil spill detection by satellite remote sensing. *Remote Sens. Environ.* **2005**, *95*, 1–13. [CrossRef]

15. Fingas, M.; Brown, C. Review of oil spill remote sensing. *Mar. Pollut. Bull.* **2014**, *83*, 9–23. [CrossRef] [PubMed]

16. Fingas, M.; Brown, C. A Review of oil spill remote sensing. *Sensors* **2017**, *18*, 91. [CrossRef] [PubMed]

17. Alpers, W.; Holt, B.; Zeng, K. Remote sensing of environment oil spill detection by imaging radars: Challenges and pitfalls. *Remote Sens. Environ.* **2017**, *201*, 133–147. [CrossRef]

18. Fingas, M.; Brown, C.E. Oil Spill Remote Sensing: A Forensics Approach. In *Standard Handbook Oil Spill Environmental Forensics*; Elsevier: Amsterdam, The Netherlands, 2016; pp. 961–981. ISBN 9780128096598.

19. Ozigis, M.S.; Kaduk, J.D.; Jarvis, C.H. Mapping terrestrial oil spill impact using machine learning random forest and Landsat 8 OLI imagery: A case site within the Niger Delta region of Nigeria. *Environ. Sci. Pollut. Res.* **2019**, *26*, 3621–3635. [CrossRef] [PubMed]

20. Pelta, R.; Carmon, N.; Ben-Dor, E. A machine learning approach to detect crude oil contamination in a real scenario using hyperspectral remote sensing. *Int. J. Appl. Earth Obs. Geoinf.* **2019**, *82*, 101901. [CrossRef]

21. Xu, J.; Wang, H.; Cui, C.; Zhao, B.; Li, B. Oil Spill Monitoring of shipborne radar image features using SVM and local adaptive threshold. *Algorithms* **2020**, *13*, 69. [CrossRef]

22. Liu, B.; Li, Y.; Li, G.; Liu, A. A spectral feature based convolutional neural network for classification of sea surface oil spill. *ISPRS Int. J. Geo-Inf.* **2019**, *8*, 160. [CrossRef]

23. Zhu, X.; Li, Y.; Zhang, Q.; Liu, B. Oil film classification using deep learning-based hyperspectral remote sensing technology. *ISPRS Int. J. Geo-Inf.* **2019**, *8*, 181. [CrossRef]

24. Park, S.H.; Jung, H.S.; Lee, M.J.; Lee, W.J.; Choi, M.J. Oil spill detection from planetscope satellite image: Application to oil spill accident near ras Al Zour area, Kuwait in august 2017. *J. Coast. Res.* **2019**, *90*, 251–260. [CrossRef]

25. Jiang, Z.; Ma, Y.; Yang, J. Inversion of the thickness of crude oil film based on an OG-CNN Model. *J. Mar. Sci. Eng.* **2020**, *8*, 653. [CrossRef]

26. Tong, S.; Liu, X.; Chen, Q.; Zhang, Z.; Xie, G. Multi-feature based ocean oil spill detection for polarimetric SAR data using random forest and the self-similarity parameter. *Remote Sens.* **2019**, *11*, 451. [CrossRef]

27. Hassani, B.; Sahebi, M.R.; Asiyabi, R.M. Oil spill four-Class classification using UAVSAR polarimetric data. *Ocean Sci. J.* **2020**, *55*, 1–11. [CrossRef]

28. Schultz, C. Monitoring and modeling the deepwater horizon oil spill: A record-breaking enterprise. *EOS Trans. Am. Geophys. Union* **2013**, *94*, 185–186. [CrossRef]

29. Fingas, M.F.; Brown, C.E. Review of oil spill remote sensing. *Spill Sci. Technol. Bull.* **1997**, *4*, 199–208. [CrossRef]

30. Zhao, J.; Temimi, M.; Ghedira, H.; Hu, C. Exploring the potential of optical remote sensing for oil spill detection in shallow coastal waters-a case study in the Arabian Gulf. *Opt. Express* **2014**, *22*, 13755. [CrossRef]

31. Garcia-Pineda, O.; Staples, G.; Jones, C.E.; Hu, C.; Holt, B.; Kourafalou, V.; Graettinger, G.; DiPinto, L.; Ramirez, E.; Streett, D.; et al. Classification of oil spill by thicknesses using multiple remote sensors. *Remote Sens. Environ.* **2020**, *236*, 111421. [CrossRef]

32. Liu, S.; Chi, M.; Zou, Y.; Samat, A.; Benediktsson, J.A.; Plaza, A. Oil spill detection via, ultitemporal optical remote sensing images: A change detection perspective. *IEEE Geosci. Remote Sens. Lett.* **2017**, *14*, 324–328. [CrossRef]

33. Zhang, T.; Guo, J.; Chi, Y.; Wang, Y. Dynamic Threshold Oil Spill Detection Algorithm for Landsat ETM+. In Proceedings of the 2019 IEEE International Geoscience and Remote Sensing Symposium (IGARSS), Yokohama, Japan, 28 July–2 August 2019; pp. 1486–1489.

34. Yin, D.; Huang, X.; Qian, W.; Huang, X.; Li, Y.; Feng, Q. Airborne validation of a new-style ultraviolet push-broom camera for ocean oil spill pollution surveillance. In *Proceedings of the Remote Sensing of the Ocean, Sea Ice, and Large Water Regions, Toulouse, France, 22–23 September 2010*; Bostater, C.R., Jr., Mertikas, S.P., Neyt, X., Velez-Reyes, M., Eds.; SPIE: Bellingham, WA, USA, 2010; Volume 7825, p. 78250I.

35. Satriano, V.; Ciancia, E.; Lacava, T.; Pergola, N.; Tramutoli, V. Improving the RST-OIL algorithm for oil spill detection under severe sun glint conditions. *Remote Sens.* **2019**, *11*, 2762. [CrossRef]

36. Kolokoussis, P.; Karathanassi, V. Oil spill detection and mapping using sentinel 2 imagery. *J. Mar. Sci. Eng.* **2018**, *6*, 4. [CrossRef]

37. Lei, F.; Wang, W.; Zhang, W.; Li, K.; Xu, Z. Oil spills tracking through texture analysis from modis imagery. In Proceedings of the IGARSS 2019—2019 IEEE International Geoscience and Remote Sensing Symposium, Yokohama, Japan, 28 July–2 August 2019; pp. 9768–9771.

38. Lacava, T.; Ciancia, E.; Coviello, I.; Di Polito, C.; Grimaldi, C.S.L.; Pergola, N.; Satriano, V.; Temimi, M.; Zhao, J.; Tramutoli, V. A MODIS-based robust satellite technique (RST) for timely detection of oil spilled areas. *Remote Sens.* **2017**, *9*, 128. [CrossRef]

39. Bhangale, U.; Durbha, S.S.; King, R.L.; Younan, N.H.; Vatsavai, R. High performance GPU computing based approaches for oil spill detection from multi-temporal remote sensing data. *Remote Sens. Environ.* **2017**, *202*, 28–44. [CrossRef]

40. Chatziantoniou, A.; Bakopoulos, V.; Papandroulakis, N.; Topouzelis, K. Detection of biogenic oil film near aquaculture sites seen by Sentinel-2 multispectral images. In *Proceedings of the Remote Sensing of the Ocean, Sea Ice, Coastal Waters, and Large Water Regions 2020*; Bostater, C.R., Neyt, X., Viallefont-Robinet, F., Eds.; SPIE: Bellingham, WA, USA, 2020; Volume 11529, p. 4.

41. Clark, R.N.; Swayze, G.A.; Leifer, I.; Livo, K.E.; Lundeen, S.; Eastwood, M.; Green, R.O.; Kokaly, R.F.; Hoefen, T.; Sarture, C.; et al. *A Method for Qualitative Mapping of Thick Oil Spills Using Imaging Spectroscopy*; U.S. Geological Survey: Reston, VA, USA, 2010.

42. De Carolis, G.; Adamo, M.; Pasquariello, G. Thickness estimation of marine oil slicks with near-infrared MERIS and MODIS imagery: The Lebanon oil spill case study. In Proceedings of the International Geoscience and Remote Sensing Symposium, Munich, Germany, 22–27 July 2012; pp. 3002–3005.

43. Sicot, G.; Lennon, M.; Miegebielle, V.; Dubucq, D. Estimation of the thickness and emulsion rate of oil spilled at sea using hyperspectral remote sensing imagery in the SWIR domain. *Int. Arch. Photogramm. Remote Sens. Spat. Inf. Sci.-ISPRS Arch.* **2015**, *40*, 445–450. [CrossRef]

44. Svejkovsky, J.; Hess, M.; Muskat, J.; Nedwed, T.J.; McCall, J.; Garcia, O. Characterization of surface oil thickness distribution patterns observed during the deepwater horizon (MC-252) oil spill with aerial and satellite remote sensing. *Mar. Pollut. Bull.* **2016**, *110*, 162–176. [CrossRef] [PubMed]

45. Sun, S.; Hu, C. The challenges of interpreting oil-water spatial and spectral contrasts for the sstimation of oil thickness: Examples from satellite and airborne measurements of the deepwater horizon oil spill. *IEEE Trans. Geosci. Remote Sens.* **2019**, *57*, 2643–2658. [CrossRef]

46. Cococcioni, M.; Corucci, L.; Masini, A.; Nardelli, F. SVME: An ensemble of support vector machines for detecting oil spills from full resolution MODIS images. *Ocean Dyn.* **2012**, *62*, 449–467. [CrossRef]

47. Corucci, L.; Nardelli, F.; Cococcioni, M. Oil spill classification from multi-spectral satellite images: Exploring different machine learning techniques. *Remote Sens. Ocean. Sea Ice Large Water Reg.* **2010**, *7825*, 782509.

48. Maianti, P.; Rusmini, M.; Tortini, R.; Dalla Via, G.; Frassy, F.; Marchesi, A.; Rota Nodari, F.; Gianinetto, M. Monitoring large oil slick dynamics with moderate resolution multispectral satellite data. *Nat. Hazards* **2014**, *73*, 473–492. [CrossRef]

49. De Carolis, G.; Adamo, M.; Pasquariello, G. On the estimation of thickness of marine oil slicks from sun-glittered, near-infrared MERIS and MODIS imagery: The lebanon oil spill case study. *IEEE Trans. Geosci. Remote Sens.* **2014**, *52*, 559–573. [CrossRef]

50. Lee, M.S.; Park, K.A.; Lee, H.R.; Park, J.J.; Kang, C.K.; Lee, M. Detection and dispersion of oil spills from satellite optical images in a coastal bay. *Int. Geosci. Remote Sens. Symp.* **2016**, *2016*, 2491–2494.

51. Li, Y.; Cui, C.; Liu, Z.; Liu, B.; Xu, J.; Zhu, X.; Hou, Y. Detection and monitoring of oil spills using moderate/high-resolution remote sensing images. *Arch. Environ. Contam. Toxicol.* **2017**, *73*, 154–169. [CrossRef] [PubMed]

52. Park, S.H.; Jung, H.S.; Lee, M.J. Oil spill mapping from Kompsat-2 high-resolution image using directional median filtering and artificial neural network. *Remote Sens.* **2020**, *12*, 253. [CrossRef]

53. Yang, J.; Wan, J.; Ma, Y.; Hu, Y. Research on object-oriented decision fusion for oil spill detection on sea surface. In Proceedings of the International Geoscience and Remote Sensing Symposium, Yokohama, Japan, 28 July–2 August 2019; pp. 9772–9775.

54. Jha, M.N.; Levy, J.; Gao, Y. Advances in remote sensing for oil spill disaster management: State-of-the-art sensors technology for oil spill surveillance. *Sensors* **2008**, *8*, 236–255. [CrossRef] [PubMed]

55. Klemas, V. Tracking oil slicks and predicting their trajectories using remote sensors and models: Case studies of the sea princess and deepwater horizon oil spills. *J. Coast. Res.* **2010**, *265*, 789–797. [CrossRef]

56. Fingas, M. The challenges of remotely measuring oil slick thickness. *Remote Sens.* **2018**, *10*, 319. [CrossRef]

57. Pisano, A.; Bignami, F.; Santoleri, R. Oil spill detection in glint-contaminated near-infrared MODIS imagery. *Remote Sens.* **2015**, *7*, 1112–1134. [CrossRef]

58. Adamo, M.; de Carolis, G.; de Pasquale, V.; Pasquariello, G. Detection and tracking of oil slicks on sun-glittered visible and near infrared satellite imagery. *Int. J. Remote Sens.* **2009**, *30*, 6403–6427. [CrossRef]

59. Bulgarelli, B.; Djavidnia, S. On MODIS retrieval of oil spill spectral properties in the marine environment. *IEEE Geosci. Remote Sens. Lett.* **2012**, *9*, 398–402. [CrossRef]

60. Chen, S.; Hu, C. In search of oil seeps in the Cariaco basin using MODIS and MERIS medium-resolution data. *Remote Sens. Lett.* **2014**, *5*, 442–450. [CrossRef]

61. Zhao, J.; Ghedira, H.; Temimi, M. Detection of oil pollution in the arabian gulf using optical remote sensing imagery. In Proceedings of the 2014 IEEE Geoscience and Remote Sensing Symposium, Québec City, QC, Canada, 13–18 July 2014; pp. 1453–1456.

62. Srivastava, H.; Singh, T.P. Assessment and development of algorithms to detection of oil spills using MODIS data. *J. Indian Soc. Remote Sens.* **2010**, *38*, 161–167. [CrossRef]

63. Lee, M.-S.; Park, K.-A.; Lee, H.-R.; Park, J.-J.; Kang, C.-K.; Lee, M. Detection and dispersion of thick and film-like oil spills in a coastal bay using satellite optical images. *IEEE J. Sel. Top. Appl. Earth Obs. Remote Sens.* **2016**, *9*, 5139–5150. [CrossRef]

64. Bayramov, E.; Kada, M.; Buchroithner, M. Monitoring oil spill hotspots, contamination probability modelling and assessment of coastal impacts in the Caspian Sea using SENTINEL-1, LANDSAT-8, RADARSAT, ENVISAT and ERS satellite sensors. *J. Oper. Oceanogr.* **2018**, *11*, 27–43. [CrossRef]

65. Arslan, N. Assessment of oil spills using Sentinel 1 C-band SAR and Landsat 8 multispectral sensors. *Environ. Monit. Assess.* **2018**, *190*, 637. [CrossRef] [PubMed]

66. Bayramov, E.; Knee, K.; Kada, M.; Buchroithner, M. Using multiple satellite observations to quantitatively assess and model oil pollution and predict risks and consequences to shoreline from oil platforms in the Caspian Sea. *Hum. Ecol. Risk Assess.* **2018**, *24*, 1501–1514. [CrossRef]

67. Zhao, D.; Cheng, X.; Zhang, H.; Zhang, H. An oil slick detection index based on Landsat 8 remote Sensing images. In Proceedings of the 2018 International Workshop on Big Geospatial Data and Data Science (BGDDS), Wuhan, China, 22–23 September 2018.

68. Taravat, A.; Del Frate, F. Development of band ratioing algorithms and neural networks to detection of oil spills using Landsat ETM+ data. *EURASIP J. Adv. Signal Process.* **2012**, *2012*, 107. [CrossRef]

69. Polychronis, K.; Vassilia, K. Detection of oil spills and underwater natural oil outflow using multispectral satellite imagery. *Int. J. Remote Sens. Appl.* **2013**, *3*, 145–154.

70. Lavrova, O.Y.; Mityagina, M.I. Satellite monitoring of oil slicks on the Black Sea surface. *Izv.-Atmos. Ocean Phys.* **2013**, *49*, 897–912. [CrossRef]

71. Althawadi, J.J.A.; Hashim, M. An approach of vicarious calibration of sentinel-2 satellite multispectral image based on spectral library for mapping oil spills. *Int. Arch. Photogramm. Remote Sens. Spat. Inf. Sci. ISPRS Arch.* **2019**, *42*, 117–121. [CrossRef]

72. Nezhad, M.M.; Groppi, D.; Laneve, G.; Marzialetti, P.; Piras, G. Oil Spill Detection Analyzing "sentinel 2" satellite images: A Persian gulf case study. In Proceedings of the World Congress on Civil, Structural, and Environmental Engineering, Budapest, Hungary, 8–10 April 2018; p. 8.

73. Cai, G.; Wu, J.; Xue, Y.; Wan, W.; Huang, X. Oil spill detection from thermal anomaly using ASTER data in Yinggehai of Hainan, China. In Proceedings of the International Geoscience and Remote Sensing Symposium, Barcelona, Spain, 23–27 July 2007; pp. 898–900.

74. Guo, G.; Liu, B.; Liu, C. Thermal infrared spectral characteristics of bunker fuel oil to determine oil-film thickness and API. *J. Mar. Sci. Eng.* **2020**, *8*, 135. [CrossRef]

75. Cai, G.; Huang, X.; Du, M.; Liu, Y. Detection of natural oil seeps signature from SST and ATI in South Yellow Sea combining ASTER and MODIS data. *Int. J. Remote Sens.* **2010**, *31*, 4869–4885. [CrossRef]

76. Hese, S.; Schmullius, C. Object-oriented oil spill contamination mapping in west Siberia with quickbird data. In *Object-Based Image Analysis*; Springer: Berlin/Heidelberg, Germany, 2008; pp. 275–290.

77. Xu, Q.; Li, X.; Wei, Y.; Tang, Z.; Cheng, Y.; Pichel, W.G. Satellite observations and modeling of oil spill trajectories in the Bohai sea. *Mar. Pollut. Bull.* **2013**, *71*, 107–116. [CrossRef] [PubMed]

78. Grimaldi, C.S.L.; Casciello, D.; Coviello, I.; Lacava, T.; Pergola, N.; Tramutoli, V. An improved RST approach for timely alert and near real time monitoring of oil spill disasters by using AVHRR data. *Nat. Hazards Earth Syst. Sci.* **2011**, *11*, 1281–1291. [CrossRef]

79. Casciello, D.; Lacava, T.; Pergola, N.; Tramutoli, V. Robust satellite techniques for oil spill detection and monitoring using AVHRR thermal infrared bands. *Int. J. Remote Sens.* **2011**, *32*, 4107–4129. [CrossRef]

80. Mihoub, Z.; Hassini, A. Remote sensing of marine oil spills using sea-viewing wide field-of-view sensor images. *Boll. Di Geofis. Teor. Ed Appl.* **2019**, *60*, 123–136.

81. Lu, Y.; Tian, Q.; Wang, X.; Zheng, G.; Li, X. Determining oil slick thickness using hyperspectral remote sensing in the Bohai sea of China. *Int. J. Digit. Earth* **2013**, *6*, 76–93. [CrossRef]

82. Shi, J.; Jiao, J.; Lu, Y.; Zhang, M.; Mao, Z.; Liu, Y. Determining spectral groups to distinguish oil emulsions from Sargassum over the Gulf of Mexico using an airborne imaging spectrometer. *ISPRS J. Photogramm. Remote Sens.* **2018**, *146*, 251–259. [CrossRef]

83. Liu, B.; Zhang, Q.; Li, Y.; Chang, W.; Zhou, M. Spatial–spectral jointed stacked auto-encoder-based deep learning for oil slick extraction from hyperspectral images. *J. Indian Soc. Remote Sens.* **2019**, *47*, 1989–1997. [CrossRef]

84. Alam, M.S.; Sidike, P. Trends in oil spill detection via hyperspectral imaging. In Proceedings of the 2012 7th International Conference on Electrical and Computer Engineering, Dhaka, Bangladesh, 20–22 December 2012; pp. 858–862.

85. Kokaly, R.F.; Couvillion, B.R.; Holloway, J.A.M.; Roberts, D.A.; Ustin, S.L.; Peterson, S.H.; Khanna, S.; Piazza, S.C. Spectroscopic remote sensing of the distribution and persistence of oil from the deepwater horizon spill in Barataria Bay marshes. *Remote Sens. Environ.* **2013**, *129*, 210–230. [CrossRef]

86. Wang, W.; Sheng, H.; Liu, S.; Chen, Y.; Wan, J.; Mao, J. An edge-preserving active contour model with bilateral filter based on hyperspectral image spectral information for oil spill segmentation. In Proceedings of the 2019 10th Workshop on Hyperspectral Imaging and Signal Processing: Evolution in Remote Sensing (WHISPERS), Amsterdam, The Netherlands, 24–26 September 2019.

87. Li, Y.; Lu, H.; Zhang, Z.; Liu, P. A novel nonlinear hyperspectral unmixing approach for images of oil spills at sea. *Int. J. Remote Sens.* **2020**, *41*, 4682–4699. [CrossRef]

88. Arellano, P.; Tansey, K.; Balzter, H.; Boyd, D.S. Detecting the effects of hydrocarbon pollution in the Amazon forest using hyperspectral satellite images. *Environ. Pollut.* **2015**, *205*, 225–239. [CrossRef]

89. Yang, J.; Wan, J.; Ma, Y.; Zhang, J.; Hu, Y. Characterization analysis and identification of common marine oil spill types using hyperspectral remote sensing. *Int. J. Remote Sens.* **2020**, *41*, 7163–7185. [CrossRef]

90. Stringer, W.J.; Dean, K.G.; Guritz, R.M.; Garbeil, H.M.; Groves, J.E.; Ahlnaes, K. Detection of petroleum spilled from the MV exxon valdez. *Int. J. Remote Sens.* **1992**, *13*, 799–824. [CrossRef]

91. Hu, C.; Li, X.; Pichel, W.G.; Muller-Karger, F.E. Detection of natural oil slicks in the NW Gulf of Mexico using MODIS imagery. *Geophys. Res. Lett.* **2009**, *36*. [CrossRef]

92. Cross, A.M. Monitoring marine oil pollution using avhrr data: Observations off the coast of kuwait and saudi arabia during january 1991. *Int. J. Remote Sens.* **1992**, *13*, 781–788. [CrossRef]

93. Chen, X.; Liu, L.; Huang, W. The detection and prediction for oil spill on the sea based on the infrared images. *Infrared Phys. Technol.* **2016**, *77*, 391–404. [CrossRef]

94. Xing, Q.; Li, L.; Lou, M.; Bing, L.; Zhao, R.; Li, Z. Observation of oil spills through Landsat thermal infrared imagery: A case of deepwater horizon. *Aquat. Procedia* **2015**, *3*, 151–156. [CrossRef]

95. Ud din, S.; Al Dousari, A.; Literathy, P. Evidence of hydrocarbon contamination from the Burgan oil field, Kuwait-Interpretations from thermal remote sensing data. *J. Environ. Manag.* **2008**, *86*, 605–615. [CrossRef]

96. Tseng, W.Y.; Chiu, L.S. AVHRR observations of Persian Gulf oil spills. In Proceedings of the International Geoscience and Remote Sensing Symposium, Pasadena, CA, USA, 8–12 August 1994; Volume 2, pp. 779–782.

97. Li, Y.; Lan, G.X.; Li, J.J.; Ma, L. Potential analysis of maritime oil spill monitoring based on MODIS thermal infrared data. In Proceedings of the International Geoscience and Remote Sensing Symposium, Cape Town, South Africa, 12–17 July 2009; Volume 3.

98. Grimaldi, C.S.L.; Coviello, I.; Lacava, T.; Pergola, N.; Tramutoli, V. A New RST-based approach for continuous oil spill detection in TIR range: The case of the deepwater horizon platform in the gulf of Mexico. In *Monitoring and Modeling the Deepwater Horizon Oil Spill: A Record-Breaking Enterprise*; American Geophysical Union (AGU): Washington, DC, USA, 2011; Volume 195, pp. 19–31.

99. Niclos, R.; Dona, C.; Valor, E.; Bisquert, M. Thermal-infrared spectral and angular characterization of crude oil and seawater emissivities for oil slick identification. *IEEE Trans. Geosci. Remote Sens.* **2014**, *52*, 5387–5395. [CrossRef]

100. Lu, Y.; Zhan, W.; Hu, C. Detecting and quantifying oil slick thickness by thermal remote sensing: A ground-based experiment. *Remote Sens. Environ.* **2016**, *181*, 207–217. [CrossRef]

101. Oulefki, A.; Trongtirakul, T.; Agaian, S.S.; Chiracharit, W. Detection and visualization of oil spill using thermal images. In *Proceedings of the Mobile Multimedia/Image Processing, Security, and Applications, 22 May 2020*; Agaian, S.S., DelMarco, S.P., Asari, V.K., Eds.; SPIE: Bellingham, WA, USA; p. 18.

102. Li, X.; Li, C.; Yang, Z.; Pichel, W. SAR imaging of ocean surface oil seep trajectories induced by near inertial oscillation. *Remote Sens. Environ.* **2013**, *130*, 182–187. [CrossRef]

103. Chen, G.; Li, Y.; Sun, G.; Zhang, Y. Application of deep networks to oil spill detection using polarimetric synthetic aperture radar images. *Appl. Sci.* **2017**, *7*, 968. [CrossRef]

104. Guo, Y.; Zhang, H.Z. Oil spill detection using synthetic aperture radar images and feature selection in shape space. *Int. J. Appl. Earth Obs. Geoinf.* **2014**, *30*, 146–157. [CrossRef]

105. Mitra, D.S.; Majumdar, T.J.; Ramakrishnan, R.; Dave, H.; Mazumder, S. Detection and monitoring of offshore oil seeps using ERS/ENVISAT SAR/ASAR data and seep-seismic studies in Krishna-Godavari offshore basin, India. *Geocarto Int.* **2013**, *28*, 404–419. [CrossRef]

106. Singha, S.; Bellerby, T.J.; Trieschmann, O. Detection and classification of oil spill and look-alike spots from SAR imagery using an Artificial Neural Network. In Proceedings of the 2012 IEEE International Geoscience and Remote Sensing Symposium, Munich, Germany, 22–27 July 2012.

107. Girard-Ardhuin, F.; Mercier, G.; Collard, F.; Garello, R. Operational oil-slick characterization by SAR imagery and synergistic data. *IEEE J. Ocean. Eng.* **2005**, *30*, 487–495. [CrossRef]

108. Taravat, A.; Del Frate, F. Weibull multiplicative model and machine learning models for full-automatic dark-spot detection from Sar images. *ISPRS Int. Arch. Photogramm. Remote Sens. Spat. Inf. Sci.* **2013**, *40*, 421–424. [CrossRef]

109. Liu, P.; Zhao, C.; Li, X.; He, M.; Pichel, W. Identification of ocean oil spills in SAR imagery based on fuzzy logic algorithm. *Int. J. Remote Sens.* **2010**, *31*, 4819–4833. [CrossRef]

110. Chehresa, S.; Amirkhani, A.; Rezairad, G.A.; Mosavi, M.R. Optimum features selection for oil spill detection in SAR image. *J. Indian Soc. Remote Sens.* **2016**, *44*, 775–787. [CrossRef]

111. Gambardella, A.; Giacinto, G.; Migliaccio, M.; Montali, A. One-class classification for oil spill detection. *Pattern Anal. Appl.* **2010**, *13*, 349–366. [CrossRef]

112. Raeisi, A.; Akbarizadeh, G.; Mahmoudi, A. combined method of an efficient cuckoo search algorithm and nonnegative matrix factorization of different zernike moment features for discrimination between oil spills and lookalikes in SAR Images. *IEEE J. Sel. Top. Appl. Earth Obs. Remote Sens.* **2018**, *11*, 4193–4205. [CrossRef]

113. Yang, Y.; Li, Y.; Zhu, X. A novel oil spill detection method from synthetic aperture radar imageries via a bidimensional empirical mode decomposition. *Acta Oceanol. Sin.* **2017**, *36*, 86–94. [CrossRef]

114. Cao, Y.; Xu, L.; Clausi, D. Exploring the potential of active learning for automatic identification of marine oil spills using 10-year (2004-2013) RADARSAT data. *Remote Sens.* **2017**, *9*, 41. [CrossRef]

115. Xu, L.; Li, J.; Brenning, A. A comparative study of different classification techniques for marine oil spill identification using RADARSAT-1 imagery. *Remote Sens. Environ.* **2014**, *141*, 14–23. [CrossRef]

116. Dabboor, M.; Singha, S.; Montpetit, B.; Deschamps, B.; Flett, D. Pre-Launch assessment of RADARSAT constellation mission medium resolution modes for sea oil slicks and lookalike discrimination. *Can. J. Remote Sens.* **2019**, *45*, 530–549. [CrossRef]

117. Kim, T.S.; Park, K.A.; Li, X.; Lee, M.; Hong, S.; Lyu, S.J.; Nam, S. Detection of the hebei spirit oil spill on SAR imagery and its temporal evolution in a coastal region of the Yellow sea. *Adv. Space Res.* **2015**, *56*, 1079–1093. [CrossRef]

118. Ozkan, C.; Osmanoglu, B.; Sunar, F.; Staples, G.; Kalkan, K.; Balık Sanlı, F. Testing the generalization efficiency of oil slick classification algorithm using multiple Sar data for deepwater horizon oil spill. *ISPRS Int. Arch. Photogramm. Remote Sens. Spat. Inf. Sci.* **2012**, *XXXIX-B7*, 67–72. [CrossRef]

119. Skrunes, S.; Brekke, C.; Eltoft, T. Characterization of marine surface slicks by radarsat-2 multipolarization features. *IEEE Trans. Geosci. Remote Sens.* **2014**, *52*, 5302–5319. [CrossRef]

120. Marghany, M. Automatic Mexico gulf oil spill detection from Radarsat-2 SAR satellite data using genetic algorithm. *Acta Geophys.* **2016**, *64*, 1916–1941. [CrossRef]

121. Zou, Y.; Shi, L.; Zhang, S.; Liang, C.; Zeng, T. Oil spill detection by a support vector machine based on polarization decomposition characteristics. *Acta Oceanol. Sin.* **2016**, *35*, 86–90. [CrossRef]

122. Li, H.Y.; Perrie, W.; Zhou, Y.Z.; He, Y.J. Oil spill detection on the ocean surface using hybrid polarimetric SAR imagery. *Sci. China Earth Sci.* **2016**, *59*, 249–257. [CrossRef]

123. Marghany, M. Automatic Detection of oil spill disasters along gulf of Mexico using RADARSAT-2 SAR data. *J. Indian Soc. Remote Sens.* **2017**, *45*, 503–511. [CrossRef]

124. Marghany, M. Oil Spill pollution automatic detection from MultiSAR satellite data using genetic algorithm. In *Advanced Geoscience Remote Sensing*; InTech: London, UK, 2014.

125. Carvalho, G.D.A.; Minnett, P.J.; Paes, E.T.; de Miranda, F.P.; Landau, L. Refined analysis of RADARSAT-2 measurements to discriminate two petrogenic oil-slick categories: Seeps versus spills. *J. Mar. Sci. Eng.* **2018**, *6*, 153. [CrossRef]

126. Wang, X.; Shao, Y.; Zhang, F.; Tian, W. Comparison of C- and L-band simulated compact polarized SAR in oil spill detection. *Front. Earth Sci.* **2019**, *13*, 351–360. [CrossRef]

127. Marghany, M. Utilization of a genetic algorithm for the automatic detection of oil spill from RADARSAT-2 SAR satellite data. *Mar. Pollut. Bull.* **2014**, *89*, 20–29. [CrossRef] [PubMed]

128. Song, D.; Ding, Y.; Li, X.; Zhang, B.; Xu, M. Ocean oil spill classification with RADARSAT-2 SAR based on an optimized wavelet neural network. *Remote Sens.* **2017**, *9*, 799. [CrossRef]

129. Singha, S.; Vespe, M.; Trieschmann, O. Automatic synthetic aperture radar based oil spill detection and performance estimation via a semi-automatic operational service benchmark. *Mar. Pollut. Bull.* **2013**, *73*, 199–209. [CrossRef]

130. Marghany, M. Automatic detection of oil spills in the gulf of Mexico from RADARSAT-2 SAR satellite data. *Environ. Earth Sci.* **2015**, *74*, 5935–5947. [CrossRef]

131. Wang, S.; Fu, X.; Zhao, Y.; Wang, H. Modification of CFAR Algorithm for Oil Spill Detection from SAR Data. *Intell. Autom. Soft Comput.* **2015**, *21*, 163–174. [CrossRef]

132. Mera, D.; Cotos, J.M.; Varela-Pet, J.G.; Rodríguez, P.; Caro, A. Automatic decision support system based on SAR data for oil spill detection. *Comput. Geosci.* **2014**, *72*, 184–191. [CrossRef]

133. Moctezuma, M.; Parmiggiani, F. Adaptive stochastic minimization for measuring marine oil spill extent in synthetic aperture radar images. *J. Appl. Remote Sens.* **2014**, *8*, 083553. [CrossRef]

134. Konik, M.; Bradtke, K. Object-oriented approach to oil spill detection using ENVISAT ASAR images. *ISPRS J. Photogramm. Remote Sens.* **2016**, *118*, 37–52. [CrossRef]

135. Akar, S.; Süzen, M.L.; Kaymakci, N. Detection and object-based classification of offshore oil slicks using ENVISAT-ASAR images. *Environ. Monit. Assess.* **2011**, *183*, 409–423. [CrossRef] [PubMed]

136. Mihoub, Z.; Hassini, A. Monitoring and identification of marine oil spills using advanced synthetic aperture radar images. *Opt. Appl.* **2014**, *44*, 433–449.

137. Senthil Murugan, J.; Parthasarathy, V. AETC: Segmentation and classification of the oil spills from SAR imagery. *Environ. Forensics* **2017**, *18*, 258–271. [CrossRef]

138. Su, T.F.; Li, H.Y.; Liu, T.X. Sea oil spill detection method using SAR imagery combined with object-Based image analysis and fuzzy logic. *Adv. Mater. Res.* **2014**, *1065–1069*, 3192–3200. [CrossRef]

139. Mera, D.; Fernández-Delgado, M.; Cotos, J.M.; Viqueira, J.R.R.; Barro, S. Comparison of a massive and diverse collection of ensembles and other classifiers for oil spill detection in SAR satellite images. *Neural Comput. Appl.* **2017**, *28*, 1101–1117. [CrossRef]

140. Yu, F.; Sun, W.; Li, J.; Zhao, Y.; Zhang, Y.; Chen, G. An improved Otsu method for oil spill detection from SAR images. *Oceanologia* **2017**, *59*, 311–317. [CrossRef]

141. Hang, L.M.; Van Truong, V. A combination method of differential evolution algorithm and neural network for automatic identification oil spill at Vietnam East Sea. *J. Geol. Resour. Eng.* **2015**, *4*, 184–193.

142. Holstein, A.; Kappas, M.; Propastin, P.; Renchin, T. Oil spill detection in the Kazakhstan sector of the Caspian sea with the help of ENVISAT ASAR data. *Environ. Earth Sci.* **2018**, *77*, 198. [CrossRef]

143. Cheng, Y.; Li, X.; Xu, Q.; Garcia-Pineda, O.; Andersen, O.B.; Pichel, W.G. SAR observation and model tracking of an oil spill event in coastal waters. *Mar. Pollut. Bull.* **2011**, *62*, 350–363. [CrossRef]

144. Zhang, Y.; Lin, H.; Liu, Q.; Hu, J.; Li, X.; Yeung, K. Oil-Spill Monitoring in the coastal waters of Hong Kong and vicinity. *Mar. Geod.* **2012**, *35*, 93–106. [CrossRef]

145. Singha, S.; Ressel, R.; Velotto, D.; Lehner, S. A Combination of Traditional and Polarimetric Features for oil spill detection using TerraSAR-X. *IEEE J. Sel. Top. Appl. Earth Obs. Remote Sens.* **2016**, *9*, 4979–4990. [CrossRef]

146. Kim, D.; Jung, H.S. Mapping oil spills from dual-polarized sar images using an artificial neural network: Application to oil spill in the kerch strait in november 2007. *Sensors* **2018**, *18*, 2237. [CrossRef]

147. Benito-Ortiz, M.C.; Mata-Moya, D.; Jarabo-Amores, M.P.; Maganto-Pascual, M.; Gomez-del-Hoyo, P.J. Multi-resolution technique-based oil spill look-alikes detection in X-band SAR data. In *Advances in Intelligent Systems and Computing*; Springer Verlag: Berlin/Heidelberg, Germany, 2019; Volume 797, pp. 737–745.

148. Nunziata, F.; de Macedo, C.R.; Buono, A.; Velotto, D.; Migliaccio, M. On the analysis of a time series of X–band TerraSAR–X SAR imagery over oil seepages. *Int. J. Remote Sens.* **2019**, *40*, 3623–3646. [CrossRef]

149. Singha, S.; Velotto, D.; Lehner, S. Near real time monitoring of platform sourced pollution using TerraSAR-X over the North Sea. *Mar. Pollut. Bull.* **2014**, *86*, 379–390. [CrossRef] [PubMed]

150. Velotto, D.; Member, S.; Migliaccio, M.; Member, S.; Nunziata, F.; Member, S.; Lehner, S. Dual-polarized TerraSAR-X data for oil-spill observation. *IEEE Trans. Geosci. Remote Sens.* **2011**, *49*, 4751–4762. [CrossRef]

151. Lupidi, A.; Staglianò, D.; Martorella, M.; Berizzi, F. Fast detection of oil spills and ships using SAR images. *Remote Sens.* **2017**, *9*, 230. [CrossRef]

152. Nunziata, F.; Buono, A.; Migliaccio, M. COSMO-SkyMed synthetic aperture radar data to observe the deepwater horizon oil spill. *Sustainability* **2018**, *10*, 3599. [CrossRef]

153. Marghany, M. Multi-objective evolutionary algorithm for oil spill detection from COSMO-SkeyMed satellite. In *Proceedings of the Lecture Notes in Computer Science (Including Subseries Lecture Notes in Artificial Intelligence and Lecture Notes in Bioinformatics)*; Springer: Berlin/Heidelberg, Germany, 2014; Volume 8584, pp. 355–371.

154. Chaudhary, V.; Kumar, S. Marine oil slicks detection using spaceborne and airborne SAR data. *Adv. Space Res.* **2020**, *66*, 854–872. [CrossRef]

155. Joseph, M.; Jayasri, P.V.; Dutta, S.; Kumari, E.V.S.S.; Prasad, A.V.V. Oil spill detection from RISAT-1 imagery using texture analysis. In Proceedings of the 2016 Asia-Pacific Microwave Conference (APMC), New Delhi, India, 5–9 December 2016.

156. Kumar, L.J.V.; Kishore, J.K.; Rao, P.K. Unsupervised classification based on decomposition of RISAT-1 images for oil spill detection. In Proceedings of the 2013 International Conference on Advances in Computing, Communications and Informatics (ICACCI), Mysore, India, 22–25 August 2013.

157. Lin, Y.; Yu, J.; Zhang, Y.; Wang, P.; Ye, Z. Dynamic analysis of oil spill in Yangtze estuary with HJ-1 imagery. In *Proceedings of the Communications in Computer and Information Science*; Springer: Berlin/Heidelberg, Germany, 2016; Volume 569, pp. 345–356.

158. Tian, W.; Bian, X.; Shao, Y.; Zhang, Z. On the detection of oil spill with China's HJ-1C SAR image. *Aquat. Procedia* **2015**, *3*, 144–150. [CrossRef]

159. Harahsheh, H.A. Oil spill detection and monitoring of Abu Dhabi coastal zone using KOMPSAT-5 SAR imagery. *Int. Arch. Photogramm. Remote Sens. Spat. Inf. Sci.* **2016**, *41*, 1115–1121. [CrossRef]

160. Kim, D. Monitoring of coastal wind and oil spill using KOMPSAT-5. In Proceedings of the 2011 3rd International Asia-Pacific Conference on Synthetic Aperture Radar, Seoul, Korea, 26–30 September 2011; pp. 1–4.

161. Prastyani, R.; Basith, A. Detecting Oil spill on Sentinel-1 imagery based on texture analysis and instantaneous wind speed estimation. In Proceedings of the 5th International Conference on Science and Technology, Yogyakarta, Indonesia, 30–31 July 2019; pp. 1–5.

162. Chaturvedi, S.K.; Banerjee, S.; Lele, S. An assessment of oil spill detection using Sentinel 1 SAR-C images. *J. Ocean Eng. Sci.* **2020**, *5*, 116–135. [CrossRef]

163. Topouzelis, K.; Singha, S. *Oil Spill Detection Using Space-Borne Sentinel-1 SAR Imagery*; Elsevier: Amsterdam, The Netherlands, 2017; ISBN 9781856179430.

164. Prastyani, R.; Basith, A. Utilisation of Sentinel-1 SAR imagery for oil spill mapping: A case study of Balikpapan Bay oil spill. *JGISE J. Geospat. Inf. Sci. Eng.* **2018**, *1*, 22–26. [CrossRef]

165. El-Magd, I.A.; Zakzouk, M.; Abdulaziz, A.M.; Ali, E.M. The potentiality of operational mapping of oil pollution in the mediterranean sea near the entrance of the suez canal using sentinel-1 SAR data. *Remote Sens.* **2020**, *12*, 1352. [CrossRef]

166. Paolini, L.; Grings, F.; Sobrino, J.; Jiménez Muñoz, J.C.; Karszenbaum, H. Radiometric correction effects in Landsat multi-date/multi-sensor change detection studies. *Int. J. Remote Sens.* **2006**, *27*, 685–704. [CrossRef]

167. Chrysoulakis, N.; Abrams, M.; Feidas, H.; Arai, K. Comparison of atmospheric correction methods using ASTER data for the area of Crete, Greece. *Int. J. Remote Sens.* **2010**, *31*, 6347–6385. [CrossRef]

168. Lu, Y.; Li, X.; Tian, Q.; Zheng, G.; Sun, S.; Liu, Y.; Yang, Q. Progress in marine oil spill optical remote sensing: Detected targets, spectral response characteristics, and theories. *Mar. Geod.* **2013**, *36*, 334–346. [CrossRef]

169. Frulla, L.A.; Milovich, J.A.; Karszenbaum, H.; Gagliardini, D.A. Radiometric corrections and calibration of SAR images. In Proceedings of the International Geoscience and Remote Sensing Symposium, Seattle, WA, USA, 6–10 July 1998; Volume 2, pp. 1147–1149.

170. Maître, H. *Processing of Synthetic Aperture Radar Images*; Willey: Hoboken, NJ, USA, 2008; ISBN 978-1-84821-024-0.

171. Yuan, L.; Ge, J.; Jiang, K.; Wang, Y. Research on efficient calibration techniques for airborne SAR systems. *Asia-Pacific Conf. Synth. Aperture Radar Proc.* **2009**, 266–269. [CrossRef]

172. Moreira, A.; Prats-Iraola, P.; Younis, M.; Krieger, G.; Hajnsek, I.; Papathanassiou, K.P. A tutorial on synthetic aperture radar. *IEEE Geosci. Remote Sens. Mag.* **2013**, *1*, 6–43. [CrossRef]

173. Loew, A.; Mauser, W. Generation of geometrically and radiometrically terrain corrected SAR image products. *Remote Sens. Environ.* **2007**, *106*, 337–349. [CrossRef]

174. Lillesand, T.; Kiefer, R.W.; Chipman, J. *Remote Sensing and Image Interpretation*; John Wiley and Sons: Hoboken, NJ, USA, 2015.

175. Argenti, F.; Lapini, A.; Alparone, L.; Bianchi, T. A tutorial on speckle reduction in synthetic aperture radar images. *IEEE Geosci. Remote Sens. Mag.* **2013**, *1*, 6–35. [CrossRef]

176. Gao, F.; Xue, X.; Sun, J.; Wang, J.; Zhang, Y. A SAR image despeckling method based on two-dimensional S transform shrinkage. *IEEE Trans. Geosci. Remote Sens.* **2016**, *54*, 3025–3034. [CrossRef]

177. Topouzelis, K.; Psyllos, A. Oil spill feature selection and classification using decision tree forest on SAR image data. *ISPRS J. Photogramm. Remote Sens.* **2012**, *68*, 135–143. [CrossRef]

178. Brekke, C.; Solberg, A.H.S. Feature extraction for oil spill detection based on SAR images. *Lect. Notes Comput. Sci.* **2005**, *3540*, 75–84.

179. Lang, H.; Zhang, X.; Xi, Y.; Zhang, X.; Li, W. Dark-spot segmentation for oil spill detection based on multifeature fusion classification in single-pol synthetic aperture radar imagery. *J. Appl. Remote Sens.* **2017**, *11*, 015006. [CrossRef]

180. Mera, D.; Bolon-Canedo, V.; Cotos, J.M.; Alonso-Betanzos, A. On the use of feature selection to improve the detection of sea oil spills in SAR images. *Comput. Geosci.* **2017**, *100*, 166–178. [CrossRef]

181. Ramalho, G.L.B.; De Medeiros, F.N.S. Improving reliability of oil spill detection systems using boosting for high-level feature selection. *Lect. Notes Comput. Sci.* **2007**, *4633*, 1172–1181.

182. Karathanassi, V.; Topouzelis, K.; Pavlakis, P.; Rokos, D. An object-oriented methodology to detect oil spills. *Int. J. Remote Sens.* **2006**, *27*, 5235–5251. [CrossRef]

183. Topouzelis, K.; Stathakis, D.; Karathanassi, V. Investigation of genetic algorithms contribution to feature selection for oil spill detection. *Int. J. Remote Sens.* **2009**, *30*, 611–625. [CrossRef]

184. Shi, L.; Zhang, X.; Seielstad, G.; Zhao, C.; He, M.X. Oil spill detection by MODIS images using fuzzy cluster and texture feature extraction. In Proceedings of the OCEANS 2007—Europe, Aberdeen, UK, 18–21 June 2007.

185. Ma, L. Support Tucker machines based marine oil spill detection using SAR images. *Indian J. Geo-Mar. Sci.* **2016**, *45*, 1445–1449.

186. Ozkan, C.; Ozturk, C.; Sunar, F.; Karaboga, D. The artificial bee colony algorithm in training artificial neural network for oil spill detection. *Neural Netw. World* **2011**, *21*, 473–492. [CrossRef]

187. Wang, Y.; Lin, M. Numerical Simulation on Oil Spilling of Submarine Pipeline and Its Evolution on Sea Surface. *Comput. Modeling Eng. Sci.* **2020**, *124*, 885–914. [CrossRef]

188. Marzialetti, P.; Laneve, G. Oil spill monitoring on water surfaces by radar L, C and X band SAR imagery: A comparison of relevant characteristics. *Int. Geosci. Remote Sens. Symp.* **2016**, *2016*, 7715–7717.

189. Hu, M.K. Visual Pattern Recognition by Moment Invariants. *IRE Trans. Inf. Theory* **1962**, *8*, 179–187.

190. Yue, G.; Xiaofeng, W. Oil spill detection by SAR images based on shape feature space. *Int. Conf. Netw. Inf. Technol. IPCSIT* **2011**, *17*, 187–194.

191. Capizzi, G.; Lo Sciuto, G.; Wozniak, M.; Damasevicius, R. A clustering based system for automated oil spill detection by satellite remote sensing. In *Artificial Intelligence and Soft Computing*; Rutkowski, L., Korytkowski, M., Scherer, R., Tadeusiewicz, R., Zadeh, L., Zurada, J., Eds.; Springer: Berlin/Heidelberg, Germany, 2016; pp. 613–623.

192. Dabbiru, L.; Samiappan, S.; Nobrega, R.A.A.; Aanstoos, J.A.; Younan, N.H.; Moorhead, R.J. Fusion of synthetic aperture radar and hyperspectral imagery to detect impacts of oil spill in Gulf of Mexico. *Int. Geosci. Remote Sens. Symp.* **2015**, *2015*, 1901–1904.

193. Zhao, P.; Yang, X.; Chen, Y.; Tong, L.; He, L. Feature extraction and classification of ocean oil spill based on SAR image. In Proceedings of the International Geoscience and Remote Sensing Symposium, Beijing, China, 10–15 July 2016; pp. 1488–1491.

194. Liu, P.; Li, Y.; Liu, B.; Chen, P.; Xu, J. Semi-automatic oil spill detection on X-band marine radar images using texture analysis, machine learning, and adaptive thresholding. *Remote Sens.* **2019**, *11*, 756. [CrossRef]

195. Chen, G.; Guo, H.; An, J. Research on SAR oil spill image classification based on DBN in small sample space. In Proceedings of the 2017 4th International Conference on Systems and Informatics (ICSAI), Hangzhou, China, 11–13 November 2017; Volume 2018, pp. 479–483.

196. Lyu, X. Oil spill detection based on features and extreme learning machine method in SAR images. In Proceedings of the 2018 3rd International Conference On Mechanical, Control and Computer Engineering, Hohhot, China, 14–16 September 2018; pp. 559–563.

197. Guo, H.; Wu, D.; An, J. Discrimination of oil slicks and lookalikes in polarimetric SAR images using CNN. *Sensors* **2017**, *17*, 1837. [CrossRef]

198. Zhang, Y.; Li, Y.; Liang, X.S.; Tsou, J. Comparison of oil spill classifications using fully and compact polarimetric SAR images. *Appl. Sci.* **2017**, *7*, 193. [CrossRef]

199. Li, X.; Nunziata, F.; Garcia, O. Oil spill detection from single- and multipolarization SAR imagery. *Compr. Remote Sens.* **2017**, *1–9*, 231–248.

200. Li, Y.; Zhang, Y.; Yuan, Z.; Guo, H.; Pan, H.; Guo, J. Marine oil spill detection based on the comprehensive use of polarimetric SAR data. *Sustainablity* **2018**, *10*, 4408. [CrossRef]

201. Song, S.; Zhao, C.; An, W.; Li, X.; Wang, C. Analysis of impacting factors on polarimetric SAR oil spill detection. *Acta Oceanol. Sin.* **2018**, *37*, 77–87. [CrossRef]

202. Salberg, A.B.; Rudjord, Ø.; Solberg, A.H.S. Oil spill detection in hybrid-polarimetric SAR images. *IEEE Trans. Geosci. Remote Sens.* **2014**, *52*, 6521–6533. [CrossRef]

203. Li, Y.; Lin, H.; Zhang, Y.; Chen, J. Comparisons of circular transmit and linear receive compact polarimetric SAR features for oil slicks discrimination. *J. Sens.* **2015**, *2015*. [CrossRef]

204. Minchew, B.; Jones, C.E.; Holt, B. Polarimetric analysis of backscatter from the deepwater horizon oil spill using l-band synthetic aperture radar. *IEEE Trans. Geosci. Remote Sens.* **2012**, *50*, 3812–3830. [CrossRef]

205. Nunziata, F.; Migliaccio, M.; Gambardella, A. Pedestal height for sea oil slick observation. *IET Radar Sonar Navig.* **2011**, *5*, 103–110. [CrossRef]

206. Migliaccio, M.; Nunziata, F.; Gambardella, A. On the co-polarized phase difference for oil spill observation. *Int. J. Remote Sens.* **2009**, *30*, 1587–1602. [CrossRef]

207. Singha, S.; Bellerby, T.J.; Trieschmann, O. Satellite oil spill detection using artificial neural networks. *IEEE J. Sel. Top. Appl. Earth Obs. Remote Sens.* **2013**, *6*, 2355–2363. [CrossRef]

208. Gibril, M.B.A.; Kalantar, B.; Al-Ruzouq, R.; Ueda, N.; Saeidi, V.; Shanableh, A.; Mansor, S.; Shafri, H.Z.M. Mapping heterogeneous urban landscapes from the fusion of digital surface model and unmanned aerial vehicle-based images using adaptive multiscale image segmentation and classification. *Remote Sens.* **2020**, *12*, 1081. [CrossRef]

209. Hamedianfar, A.; Barakat, A.; Gibril, M. Gibril Large-scale urban mapping using integrated geographic object-based image analysis and artificial bee colony optimization from worldview-3 data. *Int. J. Remote Sens.* **2019**, *40*, 6796–6821. [CrossRef]

210. Laliberte, A.S.; Browning, D.M.; Rango, A. A comparison of three feature selection methods for object-based classification of sub-decimeter resolution UltraCam-L imagery. *Int. J. Appl. Earth Obs. Geoinf.* **2012**, *15*, 70–78. [CrossRef]

211. Hamedianfar, A.; Gibril, M.B.A.; Hosseinpoor, M.; Pellikka, P.K.E. Synergistic use of particle swarm optimization, artificial neural network, and extreme gradient boosting algorithms for urban LULC mapping from WorldView-3 images. *Geocarto Int.* **2020**. [CrossRef]

212. Dash, M.; Liu, H. Feature selection for classification. *Intell. Data Anal.* **1997**, *1*, 131–156. [CrossRef]

213. Georganos, S.; Grippa, T.; Vanhuysse, S.; Lennert, M.; Shimoni, M.; Kalogirou, S.; Wolff, E. Less is more: Optimizing classification performance through feature selection in a very-high-resolution remote sensing object-based urban application. *GIScience Remote Sens.* **2018**, *55*, 221–242. [CrossRef]

214. Guyon, I.; Elisseeff, A. An introduction to variable and feature selection. *J. Mach. Learn. Res.* **2003**, *3*, 1157–1182.

215. Ma, L.; Fu, T.; Blaschke, T.; Li, M.; Tiede, D.; Zhou, Z.; Ma, X.; Chen, D. Evaluation of feature selection methods for object-based land cover mapping of unmanned aerial vehicle imagery using random forest and support vector machine classifiers. *ISPRS Int. J. Geo-Inf.* **2017**, *6*, 51. [CrossRef]

216. Colkesen, I.; Kavzoglu, T. Selection of optimal object features in object-based image analysis using filter-based algorithms. *J. Indian Soc. Remote Sens.* **2018**, *46*, 1233–1242. [CrossRef]

217. Shanableh, A.; Al-Ruzouq, R.; Gibril, M.B.A.; Flesia, C.; AL-Mansoori, S. Spatiotemporal mapping and monitoring of whiting in the semi-enclosed gulf using moderate resolution imaging spectroradiometer (MODIS) time series images and a generic ensemble tree-based model. *Remote Sens.* **2019**, *11*, 1193. [CrossRef]

218. Zhou, Y.; Chen, Y.; Feng, L.; Zhang, X.; Shen, Z.; Zhou, X. Supervised and adaptive feature weighting for object-based classification on satellite images. *IEEE J. Sel. Top. Appl. Earth Obs. Remote Sens.* **2018**, *11*, 3224–3234. [CrossRef]

219. Wolff, S.; O'Donncha, F.; Chen, B. Statistical and machine learning ensemble modelling to forecast sea surface temperature. *J. Mar. Syst.* **2020**, *208*, 103347. [CrossRef]

220. Guirado, E.; Tabik, S.; Rivas, M.L.; Alcaraz-Segura, D.; Herrera, F. Whale counting in satellite and aerial images with deep learning. *Sci. Rep.* **2019**, *9*, 1–12. [CrossRef]

221. Li, X.; Liu, B.; Zheng, G.; Ren, Y.; Zhang, S.; Liu, Y.; Gao, L.; Liu, Y.; Zhang, B.; Wang, F. Deep learning-based information mining from ocean remote sensing imagery. *Natl. Sci. Rev.* **2020**, 1–22. [CrossRef]

222. Prakash, N.; Manconi, A.; Loew, S. Mapping landslides on EO data: Performance of deep learning models vs. Traditional machine learning models. *Remote Sens.* **2020**, *12*, 346. [CrossRef]

223. Shahabi, H.; Shirzadi, A.; Ghaderi, K.; Omidvar, E.; Al-Ansari, N.; Clague, J.J.; Geertsema, M.; Khosravi, K.; Amini, A.; Bahrami, S.; et al. Flood detection and susceptibility mapping using Sentinel-1 remote sensing data and a machine learning approach: Hybrid intelligence of bagging ensemble based on K-Nearest Neighbor classifier. *Remote Sens.* **2020**, *12*, 266. [CrossRef]

224. Sharma, R.; Rani, S.; Memon, I. A smart approach for fire prediction under uncertain conditions using machine learning. *Multimed. Tools Appl.* **2020**, *79*, 1–14. [CrossRef]

225. Kalantar, B.; Ueda, N.; Saeidi, V.; Ahmadi, K.; Halin, A.A.; Shabani, F. Landslide Susceptibility Mapping: Machine and ensemble learning based on remote sensing big data. *Remote Sens.* **2020**, *12*, 1737. [CrossRef]

226. Xavier, L.C.P.; Carvalho, T.M.N.; Filho, J.D.P.; de Souza Filho, F.d.A.; da Silva, S.M.O. Use of machine learning in evaluation of drought perception in irrigated agriculture: The case of an irrigated perimeter in Brazil. *Water* **2020**, *12*, 1546. [CrossRef]

227. Mazzia, V.; Comba, L.; Khaliq, A.; Chiaberge, M.; Gay, P. UAV and machine learning based refinement of a satellite-driven vegetation index for precision agriculture. *Sensors* **2020**, *20*, 2530. [CrossRef]

228. Al-najjar, H.A.H.; Kalantar, B.; Pradhan, B.; Saeidi, V. Land Cover Classification from fused DSM and UAV Images Using Convolutional Neural Networks. *Remote Sens.* **2019**, *11*, 1461. [CrossRef]

229. Gibril, M.B.A.; Idrees, M.O.; Yao, K.; Shafri, H.Z.M. Integrative image segmentation optimization and machine learning approach for high quality land-use and land-cover mapping using multisource remote sensing data. *J. Appl. Remote Sens.* **2018**, *12*. [CrossRef]

230. Shen, H.; Jiang, Y.; Li, T.; Cheng, Q.; Zeng, C.; Zhang, L. Deep learning-based air temperature mapping by fusing remote sensing, station, simulation and socioeconomic data. *Remote Sens. Environ.* **2020**, *240*, 111692. [CrossRef]

231. Yang, G.; Lee, H.; Lee, G. A hybrid deep learning model to forecast particulate matter concentration levels in Seoul, South Korea. *Atmosphere* **2020**, *11*, 348. [CrossRef]

232. Franch, G.; Nerini, D.; Pendesini, M.; Coviello, L.; Jurman, G.; Furlanello, C. Precipitation nowcasting with orographic enhanced stacked generalization: Improving deep learning predictions on extreme events. *Atmosphere* **2020**, *11*, 267. [CrossRef]

233. Mitchell, T.M. *Machine Learning*; McGraw-Hill: New York, NY, USA, 1997.

234. Misra, A.; Balaji, R. Simple approaches to oil spill detection using sentinel application platform (SNAP)-Ocean application tools and texture analysis: A Comparative Study. *J. Indian Soc. Remote Sens.* **2017**, *45*, 1065–1075. [CrossRef]

235. Gil, P.; Alacid, B. Oil spill detection in terma-side-looking airborne radar images using image features and region segmentation. *Sensors* **2018**, *18*, 151. [CrossRef] [PubMed]

236. Ajadi, O.A.; Meyer, F.J.; Tello, M.; Ruello, G. Oil spill detection in synthetic aperture radar images using lipschitz-regularity and multiscale techniques. *IEEE J. Sel. Top. Appl. Earth Obs. Remote Sens.* **2018**, *11*, 2389–2405. [CrossRef]

237. Garcia-Pineda, O.; MacDonald, I.R.; Li, X.; Jackson, C.R.; Pichel, W.G. Oil spill mapping and measurement in the gulf of mexico with Textural Classifier Neural Network Algorithm (TCNNA). *IEEE J. Sel. Top. Appl. Earth Obs. Remote Sens.* **2013**, *6*, 2517–2525. [CrossRef]

238. Del Frate, F.; Latini, D.; Scappiti, V. On neural networks algorithms for oil spill detection when applied to C- and X-band SAR. *Int. Geosci. Remote Sens. Symp.* **2017**, *2017*, 5249–5251.

239. Gogate, P.U.; Desai, P.; Gawde, M.; Harne, S. Classification and Detection of Oil Spills Using Artificial Neural Network. *Int. J. Adv. Res. Comput. Commun. Eng.* **2016**, *5*, 62–64.

240. Avezzano, R.G.; Velotto, D.; Soccorsi, M.; Del Frate, F.; Lehner, S. Neural networks for oil spill detection using TerraSAR-X data. In *Proceedings of the SAR Image Analysis, Modeling, and Techniques XI*; SPIE: Bellingham, WA, USA, 2011; Volume 8179, p. 817911.

241. Wan, J.; Cheng, Y. Remote sensing monitoring of gulf of Mexico oil spill using ENVISAT ASAR images. *Int. Conf. Geoinf.* **2013**, 1–5. [CrossRef]

242. Joseph, M.; Jayasri, P.V.; Dutta, S.; Kumari, E.V.S.S.; Prasad, A.V.V. Oil spill detection from RISAT-1 imagery using texture analysis. In Proceedings of the Asia-Pacific Microwave Conference, Kyoto, Japan, 6–9 November 2019; Institute of Electrical and Electronics Engineers: Piscataway, NJ, USA, 2017.

243. Zisimopoulos, M.; Kyriou, A.; Nikolakopoulos, K.G. Synergy of Copernicus optical and radar data for oil spill detection. In *Proceedings of the Earth Resources and Environmental Remote Sensing/GIS Applications X*; Schulz, K., Nikolakopoulos, K.G., Michel, U., Eds.; SPIE: Bellingham, WA, USA, 2019; Volume 11156, p. 37.

244. Fausett, L. Fundamentals of neural networks: Architectures, algorithms and applications. *J. Chromatogr. B Analyt. Technol. Biomed. Life Sci.* **2005**, *814*, 315–323.

245. Fausett, L. *Fundamentals of Neural Networks*; Prentice-Hall: Upper Saddle River, NJ, USA, 1994; ISBN 978-0-13-334186-7.

246. Fausett, L. *Fundamentals of Neural Networks: Architectures, Algorithms and Applications Fundamentals of Neural Networks: Architectures, Algorithms and Applications*; Pearson Education: Cranbury, NJ, USA, 2005; Volume 814.

247. Cortes, C.; Vapnik, V. Support-vector networks. *Mach. Learn.* **1995**, *20*, 273–297. [CrossRef]

248. Vapnik, V.N. *The Nature of Statistical Learning Theory*; Springer: New York, NY, USA, 1995.

249. Kavzoglu, T.; Colkesen, I. A kernel functions analysis for support vector machines for land cover classification. *Int. J. Appl. Earth Obs. Geoinf.* **2009**, *11*, 352–359. [CrossRef]

250. Chi, M.; Feng, R.; Bruzzone, L. Classification of hyperspectral remote-sensing data with primal SVM for small-sized training dataset problem. *Adv. Space Res.* **2008**, *41*, 1793–1799. [CrossRef]

251. Burbidge, R.; Trotter, M.; Buxton, B.; Holden, S. Drug design by machine learning: Support vector machines for pharmaceutical data analysis. *Comput. Chem.* **2001**, *26*, 5–14. [CrossRef]

252. Breiman, L.; Friedman, J.H.; Olshen, R.A.; Stone, C.J. *Classification and Regression Trees*; Wadsworth: Monterey, CA, USA, 1984.

253. Ghose, M.K.; Pradhan, R.; Ghose, S.S. Decision tree classification of remotely sensed satellite data using spectral separability matrix. *Int. J. Adv. Comput. Sci. Appl.* **2010**, *1*, 93–101.

254. James, A.P. *Deep Learning Classifiers with Memristive Networks*; Springer: Berlin/Heidelberg, Germany, 2020; Volume 14, ISBN 978-3-030-14522-4.

255. Zhang, L.; Zhang, L.; Du, B. Deep learning for remote sensing data: A technical tutorial on the state of the art. *IEEE Geosci. Remote Sens. Mag.* **2016**, *4*, 22–40. [CrossRef]

256. Deng, L.; Way, O.M.; Yu, D.; Way, O.M. Deep learning: Methods and applications. *Signal Process.* **2014**, *7*, 197–387.

257. Jiao, Z.; Jia, G.; Cai, Y. A new approach to oil spill detection that combines deep learning with unmanned aerial vehicles. *Comput. Ind. Eng.* **2019**, *135*, 1300–1311. [CrossRef]

258. Yaohua, X.; Xudong, M. A SAR oil spill image recognition method based on densenet convolutional neural network. In Proceedings of the 2019 International Conference on Intelligent Robots and Systems, Macau, China, 3–8 November 2019; pp. 78–81.

259. Chen, Y.; Li, Y.; Wang, J. An end-to-end oil-spill monitoring method for multisensory satellite images based on deep semantic segmentation. *Sensors* **2020**, *20*, 725. [CrossRef]

260. Krestenitis, M.; Orfanidis, G.; Ioannidis, K.; Avgerinakis, K.; Vrochidis, S.; Kompatsiaris, I. Oil spill identification from satellite images using deep neural networks. *Remote Sens.* **2019**, *11*, 1762. [CrossRef]

261. Zhang, J.; Feng, H.; Luo, Q.; Li, Y.; Wei, J.; Li, J. Oil spill detection in quad-polarimetric SAR Images using an advanced convolutional neural network based on SuperPixel model. *Remote Sens.* **2020**, *12*, 944. [CrossRef]

262. Guo, H.; Wei, G.; An, J. Dark spot detection in SAR images of oil spill using segnet. *Appl. Sci.* **2018**, *8*, 2670. [CrossRef]

263. Bazine, R.; Wu, H.; Boukhechba, K. Semantic segmentation of SLAR imagery with convolutional LSTM selectional autoencoders. *Remote Sens.* **2019**, *11*, 1–22.

264. Orfanidis, G.; Ioannidis, K.; Avgerinakis, K.; Vrochidis, S.; Kompatsiaris, I. A deep neural network for oil spill semantic segmentation in Sar images. In Proceedings of the International Conference on Image Processing, Athens, Greece, 7–10 October 2018; pp. 3773–3777.

265. Cantorna, D.; Dafonte, C.; Iglesias, A.; Arcay, B. Oil spill segmentation in SAR images using convolutional neural networks. A comparative analysis with clustering and logistic regression algorithms. *Appl. Soft Comput. J.* **2019**, *84*, 105716. [CrossRef]

266. Lecun, Y.; Bengio, Y.; Hinton, G. Deep learning. *Nature* **2015**, *521*, 436–444. [CrossRef]

267. Lecun, Y.; Bottou, L.; Bengio, Y.; Ha, P. LeNet. *Proc. IEEE* **1998**, 1–46.

268. Goodfellow, I.; Bengio, Y.; Courville, A.; Bengio, Y. *Deep Learning*; MIT Press: Cambridge, UK, 2016; Volume 1.

269. Xiong, Y.; Zhou, H. Oil spills identification in SAR image based on convolutional neural network. In Proceedings of the 14th International Conference on Computer Science and Education, Toronto, ON, Canada, 19–21 August 2019; pp. 667–670.

270. Zeng, K.; Wang, Y. A deep convolutional neural network for oil spill detection from spaceborne SAR images. *Remote Sens.* **2020**, *12*, 1015. [CrossRef]

271. Song, D.; Zhen, Z.; Wang, B.; Li, X.; Gao, L.; Wang, N.; Xie, T.; Zhang, T. A novel marine oil spillage identification scheme based on convolution neural network feature extraction from fully polarimetric SAR imagery. *IEEE Access* **2020**, *8*, 59801–59820. [CrossRef]

272. Nieto-Hidalgo, M.; Gallego, A.J.; Gil, P.; Pertusa, A. Two-stage convolutional neural network for ship and spill detection using SLAR images. *IEEE Trans. Geosci. Remote Sens.* **2018**, *56*, 5217–5230. [CrossRef]

273. Huang, H.; Wang, C.; Liu, S.; Sun, Z.; Zhang, D.; Liu, C.; Jiang, Y.; Zhan, S.; Zhang, H.; Xu, R. Single spectral imagery and faster R-CNN to identify hazardous and noxious substances spills. *Environ. Pollut.* **2020**, *258*, 113688. [CrossRef]

274. Krestenitis, M.; Orfanidis, G.; Ioannidis, K.; Avgerinakis, K.; Vrochidis, S.; Kompatsiaris, I. Early identification of oil spills in satellite images using deep CNNs. In Proceedings of the International Conference on Multimedia Modeling, Thessaloniki, Greece, 8–11 January 2019; pp. 424–435.

275. Li, Y.; Yang, X.; Ye, Y.; Cui, L.; Jia, B.; Jiang, Z.; Wang, S. Detection of oil spill through fully convolutional network. In *Communications in Computer and Information Science*; Springer: Berlin/Heidelberg, Germany, 2018; Volume 848, pp. 353–362.

276. Bianchi, F.M.; Espeseth, M.M.; Borch, N. Large-scale detection and categorization of oil spills from SAR images with deep learning. *Remote Sens.* **2020**, *12*, 2260. [CrossRef]

277. Temitope, S.; Balogun, A.; Wan, K.B. A novel deep learning instance segmentation model for automated marine oil spill detection. *ISPRS J. Photogramm. Remote Sens.* **2020**, *167*, 190–200. [CrossRef]

278. Gallego, A.-J.; Gil, P.; Pertusa, A.; Fisher, R. Segmentation of oil spills on side-looking airborne radar imagery with autoencoders. *Sensors* **2018**, *18*, 797. [CrossRef]

279. Oprea, S.O.; Gil, P.; Mira, D.; Alacid, B. Candidate oil spill detection in SLAR data a recurrent neural network-based approach. In Proceedings of the 6th International Conference on Pattern Recognition Applications and Methods, Porto, Portugal, 24–26 February 2017; pp. 372–377.

280. Yu, X.; Zhang, H.; Luo, C.; Qi, H.; Ren, P. Oil spill segmentation via adversarial f-divergence learning. *IEEE Trans. Geosci. Remote Sens.* **2018**, *56*, 4973–4988. [CrossRef]

281. Song, J.; Gao, S.; Zhu, Y.; Ma, C. A survey of remote sensing image classification based on CNNs. *Big Earth Data* **2019**, *3*, 232–254. [CrossRef]

282. Wang, L.; Xu, X.; Dong, H.; Gui, R.; Pu, F. Multi-pixel simultaneous classification of PolSAR image using convolutional neural networks. *Sensors* **2018**, *18*, 769. [CrossRef] [PubMed]

283. Zeiler, M.D.; Fergus, R. Stochastic pooling for regularization of deep convolutional neural networks. In Proceedings of the 1st International Conference on Learning Representation, Scottsdale, AZ, USA, 2–4 May 2013.

284. Simonyan, K.; Zisserman, A. Very deep convolutional networks for large-scale image recognition. *arXiv* **2014**, arXiv:1409.1556.

285. He, K.; Zhang, X.; Ren, S.; Sun, J. Spatial pyramid pooling in deep convolutional networks for visual recognition. *IEEE Trans. Pattern Anal. Mach. Intell.* **2015**, *37*, 1904–1916. [CrossRef] [PubMed]

286. Chen, L.C.; Papandreou, G.; Kokkinos, I.; Murphy, K.; Yuille, A.L. DeepLab: Semantic image segmentation with deep convolutional nets, atrous convolution, and fully connected CRFs. *IEEE Trans. Pattern Anal. Mach. Intell.* **2018**, *40*, 834–848. [CrossRef]

287. Girshick, R.; Donahue, J.; Darrell, T.; Malik, J. Rich feature hierarchies for accurate object detection and semantic segmentation. In Proceedings of the IEEE Conference on Computer Vision and Pattern Recognition (CVPR), Columbus, OH, USA, 24–27 June 2014; pp. 580–587.

288. Zhang, Z.; Guo, W.; Zhu, S.; Yu, W. Toward arbitrary-oriented ship detection with rotated region proposal and discrimination networks. *IEEE Geosci. Remote Sens. Lett.* **2018**, *15*, 1745–1749. [CrossRef]

289. Ren, S.; He, K.; Girshick, R.; Sun, J. Faster R-CNN: Towards real-time object detection with region proposal networks. *IEEE Trans. Pattern Anal. Mach. Intell.* **2017**, *39*, 1137–1149. [CrossRef] [PubMed]

290. He, K.; Gkioxari, G.; Dollár, P.; Girshick, R. Mask R-CNN. *IEEE Trans. Pattern Anal. Mach. Intell.* **2020**, *42*, 386–397. [CrossRef] [PubMed]

291. Redmon, J.; Divvala, S.; Girshick, R.; Farhadi, A. You only look once: Unified, real-time object detection. In Proceedings of the 2016 IEEE Conference on Computer Vision and Pattern Recognition, Las Vegas, NV, USA, 27–30 June 2016; pp. 779–788.

292. Liu, W.; Anguelov, D.; Erhan, D.; Szegedy, C.; Reed, S.; Fu, C.Y.; Berg, A.C. SSD: Single shot multibox detector. *Lect. Notes Comput. Sci.* **2016**, *9905*, 21–37.

293. Nie, X.; Duan, M.; Ding, H.; Hu, B.; Wong, E.K. Attention mask R-CNN for ship detection and segmentation from remote sensing images. *IEEE Access* **2020**, *8*, 9325–9334. [CrossRef]

294. Yao, Y.; Jiang, Z.; Zhang, H.; Zhao, D.; Cai, B. Ship detection in optical remote sensing images based on deep convolutional neural networks. *J. Appl. Remote Sens.* **2017**, *11*, 1. [CrossRef]

295. Zhai, M.; Liu, H.; Sun, F.; Zhang, Y. Ship detection based on faster R-CNN network in optical remote sensing images. In Proceedings of the Lecture Notes in Electrical Engineering; Springer: Berlin/Heidelberg, Germany, 2020; Volume 586, pp. 22–31.

296. Dong, Z.; Lin, B. Learning a robust CNN-based rotation insensitive model for ship detection in VHR remote sensing images. *Int. J. Remote Sens.* **2020**, *41*, 3614–3626. [CrossRef]

297. Ruiz-Santaquiteria, J.; Bueno, G.; Deniz, O.; Vallez, N.; Cristobal, G. Semantic versus instance segmentation in microscopic algae detection. *Eng. Appl. Artif. Intell.* **2020**, *87*, 103271. [CrossRef]

298. Wang, L. Advances in natural computation, fuzzy systems and nnowledge discovery. In *Advances in Intelligent Systems and Computing*; Liu, Y., Wang, L., Zhao, L., Yu, Z., Eds.; Springer: Cham, Switzerland, 2020; Volume 1074, ISBN 978-3-030-32455-1.

299. Long, J.; Shelhamer, E.; Darrell, T. Fully convolutional networks for semantic segmentation. In Proceedings of the 2015 IEEE Conference on Computer Vision and Pattern Recognition, Boston, MA, USA, 7–12 June 2015; pp. 3431–3440.

300. Jegou, S.; Drozdzal, M.; Vazquez, D.; Romero, A.; Bengio, Y. The one hundred layers tiramisu: Fully convolutional DenseNets for semantic segmentation. In Proceedings of the IEEE Computer Society Conference on Computer Vision and Pattern Recognition Workshops, Honolulu, HI, USA, 21–26 July 2017; pp. 1175–1183.

301. Ronneberger, O.; Fischer, P.; Brox, T. U-net: Convolutional networks for biomedical image segmentation. In Proceedings of the Lecture Notes in Computer Science; Springer: Berlin/Heidelberg, Germany, 2015; Volume 9351, pp. 234–241.

302. Zhao, H.; Shi, J.; Qi, X.; Wang, X.; Jia, J. PSPNet. In Proceedings of the 30th IEEE Conference on Computer Vision and Pattern Recognition, Honolulu, HI, USA, 22–25 July 2017; pp. 6230–6239.

303. Badrinarayanan, V.; Kendall, A.; Cipolla, R. SegNet: A deep convolutional encoder-Decoder architecture for image segmentation. *IEEE Trans. Pattern Anal. Mach. Intell.* **2017**, *39*, 2481–2495. [CrossRef]

304. Lin, G.; Milan, A.; Shen, C.; Reid, I. RefineNet: Multi-path refinement networks for high-resolution semantic segmentation. In Proceedings of the 30th IEEE Conference on Computer Vision and Pattern Recognition, Honolulu, HI, USA, 22–25 July 2017; Volume 2017, pp. 5168–5177.

305. Li, H.; Xiong, P.; An, J.; Wang, L. Pyramid attention network for semantic segmentation. In Proceedings of the 2018 British Machine Vision Conference, Newcastle, UK, 3–6 September 2018.

306. Chen, L.-C.; Papandreou, G.; Kokkinos, I.; Murphy, K.; Yuille, A.L. Semantic Image Segmentation with Deep Convolutional Nets and Fully Connected CRFs. *arXiv* **2014**, arXiv:1412.7062, 1–12.

307. Yu, C.; Wang, J.; Peng, C.; Gao, C.; Yu, G.; Sang, N. Learning a Discriminative Feature Network for Semantic Segmentation. In Proceedings of the IEEE Computer Society Conference on Computer Vision and Pattern Recognition, Salt Lake City, UT, USA, 18–22 June 2018; pp. 1857–1866.

308. Topouzelis, K.N. Oil spill detection by SAR images: Dark formation detection, feature extraction and classification algorithms. *Sensors* **2008**, *8*, 6642–6659. [CrossRef]

309. Hinton, G.E.; Zemel, R.S. Autoencoders, minimum description length and helmholtz free energy. *Adv. Neural Inf. Process. Syst.* **1994**, *6*, 3–10.

310. Dong, G.; Liao, G.; Liu, H.; Kuang, G. A review of the autoencoder and its variants: A comparative perspective from target recognition in synthetic-aperture radar images. *IEEE Geosci. Remote Sens. Mag.* **2018**, *6*, 44–68. [CrossRef]

311. Parikh, H.; Patel, S.; Patel, V. *Classification of SAR and PolSAR Images Using Deep Learning: A Review*; Taylor and Francis: Abingdon, UK, 2020; Volume 11, ISBN 0000000242806.

312. Maxwell, A.E.; Warner, T.A.; Fang, F. Implementation of machine-learning classification in remote sensing: An applied review. *Int. J. Remote Sens.* **2018**, *39*, 2784–2817. [CrossRef]

313. Kubat, M.; Holte, R.C.; Matwin, S. Machine learning for the detection of oil spills in satellite radar images. *Mach. Learn.* **1998**, *30*, 195–215. [CrossRef]

314. SpaceNet. Available online: https://spacenetchallenge.github.io/ (accessed on 24 August 2020).

315. EMSA Earth Observation Services CleanSeaNet service.EMSA European Maritime Safety Agency. Available online: http://emsa.europa.eu/csn-menu/csn-service.html (accessed on 2 September 2020).